Article

Eisosomes Are Dynamic Plasma Membrane Domains Showing Pil1-Lsp1 Heteroligomer Binding Equilibrium

Agustina Olivera-Couto,[1] Valentina Salzman,[1] Milagros Mailhos,[1] Michelle A. Digman,[2,3] Enrico Gratton,[2,*] and Pablo S. Aguilar[1,*]

[1]Laboratorio de Biología Celular de Membranas, Institut Pasteur de Montevideo, Montevideo, Uruguay; [2]Laboratory for Fluorescence Dynamics, Department of Biomedical Engineering, University of California-Irvine, Irvine, California; and [3]Centre for Bioactive Discovery in Health and Ageing, School of Science and Technology, University of New England, Armidale, Australia

ABSTRACT Eisosomes are plasma membrane domains concentrating lipids, transporters, and signaling molecules. In the budding yeast *Saccharomyces cerevisiae*, these domains are structured by scaffolds composed mainly by two cytoplasmic proteins Pil1 and Lsp1. Eisosomes are immobile domains, have relatively uniform size, and encompass thousands of units of the core proteins Pil1 and Lsp1. In this work we used fluorescence fluctuation analytical methods to determine the dynamics of eisosome core proteins at different subcellular locations. Using a combination of scanning techniques with autocorrelation analysis, we show that Pil1 and Lsp1 cytoplasmic pools freely diffuse whereas an eisosome-associated fraction of these proteins exhibits slow dynamics that fit with a binding-unbinding equilibrium. Number and brightness analysis shows that the eisosome-associated fraction is oligomeric, while cytoplasmic pools have lower aggregation states. Fluorescence lifetime imaging results indicate that Pil1 and Lsp1 directly interact in the cytoplasm and within the eisosomes. These results support a model where Pil1-Lsp1 heterodimers are the minimal eisosomes building blocks. Moreover, individual-eisosome fluorescence fluctuation analysis shows that eisosomes in the same cell are not equal domains: while roughly half of them are mostly static, the other half is actively exchanging core protein subunits.

INTRODUCTION

Compartmentalization of the plasma membrane allows both prokaryote and eukaryote cells to efficiently coordinate essential functions such as cell division and trafficking of materials and information (1,2). Above the micron scale, plasma membrane heterogeneity is evident in eukaryotic-polarized cells where apical and basolateral domains, formed by the polarized trafficking machinery and maintained by tight junctions, ascertain epithelial functional identity (3). Below the micron scale, plasma membrane nanodomains exhibit high diversity of temporal and spatial scales extending from tens to hundreds of nanometers and from milliseconds to minutes and even permanent residency within a cell lifespan (4,5). Our understanding of nanoscale plasma membrane domains composition has been deeply enriched by live microscopy studies using fluorescently labeled proteins and lipids. These studies have unequivocally shown the existence of plasma membrane nanodomains, and their mechanisms of formation, maintenance, and disassembly are under intense debate and study (2,6). Proposed mechanisms focus on confinement within fences formed by membrane proteins anchored to the cytoskeleton, preferential chemical associations among proteins and lipids, and clustering of protein and lipids by membrane-associated scaffolding proteins (2,7).

The plasma membrane of the yeast *Saccharomyces cerevisiae*, contains at least a dozen different nanodomains that exhibit different morphologies and dynamic behaviors (8). Among them, there are topographically distinctive domains, which are shaped as 200–400-nm long and 50-nm-deep invaginated furrows (9,10). Depending on the cell size, there are between 20 and 50 furrows per cell, showing an even distribution and a rather constant density of 0.33 ± 0.06 domains/μm^2 cell surface. These plasma membrane furrows concentrate at least 23 different proteins including nutrient transporters such as Can1 and Tat2 (11,12), membrane-associated signaling proteins such as Pkh1 and Pkh2 kinases (13,14), and the target of rapamycin complex 2 (TORC2) effectors Slm1 and Slm2 (15,16). Two highly abundant membrane-associated proteins, Pil1 and Lsp1, constitute the structural core of these domains (9,17). For each one of these invaginated furrows, it is estimated that 2000–5000 units of both Pil1 and Lsp1 are assembled on the cytoplasmic side of the plasma membrane (17). Pil1 and Lsp1 assemblies have been named “eisosomes” (17) whereas the plasma membrane domains concentrating Can1 and other nutrient

Submitted September 26, 2014, and accepted for publication February 12, 2015.

*Correspondence: pablo.aguilar@pasteur.edu.uy or egratton22@gmail.com

Valentina Salzman’s current address is Instituto de Investigaciones Biológicas, San Martin, Buenos Aires, Argentina.

Editor: Paul Wiseman.

0006-3495/15/04/1633/12 $2.00

http://dx.doi.org/10.1016/j.bpj.2015.02.011

transporters have been named "membrane compartment occupied by Can1" (MCC) (12). Eisosomes and MCCs both constitute the same subcellular structure: the plasma membrane furrowlike invagination. For simplicity, we will use the term "eisosomes" to describe the plasma membrane invaginated furrows and the proteins that partition within. Eisosomes are immobile domains that are formed de novo in the buds of dividing cells (18). The cytoplasmic pools of the core proteins Pil1 and Lsp1 join the plasma membrane of growing buds in a coordinated fashion with other eisosome components. *PIL1* expression oscillates in synchronicity with the cell cycle, matching high expression levels with eisosome formation and buds' plasma membrane growth (18). Pil1 is a major player in eisosomes assembly and maintenance. Deletion of *PIL1* leads to disappearance of furrow membrane invaginations and dramatic relocation of all other known eisosome components: integral membrane proteins spread along the plasma membrane and membrane-associated proteins, including Lsp1, fall into the cytoplasm. In the absence of Pil1, very few and large clusters, referred to as "eisosome remnants", persist at the plasma membrane concentrating a fraction of the original eisosomal proteins (17).

Remarkably, this phenotype is not mimicked by the absence of Lsp1, which is 74% identical in amino-acid sequence to Pil1. Lsp1 and Pil1 are bar/amphyphysin/rvs (BAR) domain-containing proteins able to form a membrane-bound scaffold imposing membrane curvature in vitro and in vivo (19–21). Besides all these extensive studies, the molecular mechanism of eisosome formation and maintenance are still poorly understood. Other eisosome components such as the tetraspanning membrane protein Nce102 and the membrane-associated protein Seg1 are required for efficient incorporation of Pil1 into eisosomes, but their molecular structures and mechanisms of action are still unknown (22,23). Crystallographic studies show that Lsp1, like canonical BAR domain proteins, forms a homodimer in vitro (20). However, whether the cytoplasmic pools of Pil1 and Lsp1 form homo- and/or heterodimers, or even higher-order preassembled units in vivo, remains uncertain. In vitro, Pil1 and Lsp1 are able to directly bind to lipids, but it is unknown whether their cytoplasmic pools are either already bound to intracellular membranes or behave as free diffusing entities. To further contribute to our understanding of eisosome assembly and maintenance mechanisms, we have focused on Pil1 and Lsp1, addressing quantitative aspects of these proteins' dynamics in live cells.

In this work, by using fluorescence fluctuation analytical methods we have determined the dynamic behavior of cytoplasmic Pil1 and Lsp1 in vivo. We have also found that roughly half of the eisosome population contains a dynamic pool of Pil1 and Lsp1. Number and brightness (N&B) and fluorescence correlation spectroscopy (FCS) analysis show that these dynamic pools are oligomeric with slow dynamics that fit with a binding-unbinding equilibrium. Finally, using fluorescence lifetime imaging on live cells, we demonstrated that Pil1 and Lsp1 form heterodimers in the cytoplasm and within the eisosomes.

MATERIALS AND METHODS

The *S. cerevisiae* strains, reagents, media, and growth conditions, Western blotting, microscope setups, mathematics, and data processing are detailed in the Supporting Material.

RESULTS

Eisosome core proteins Pil1 and Lsp1 exhibit diffusive behavior within the cytoplasm

In mitotically active yeast cells, eisosomes are formed de novo in the growing buds by progressive deposition of Seg1, Pil1, Lsp1, and the rest of eisosomal components (18,19,23). Before the bud reaches its final size, well before cytokinesis, deposition of Pil1 (and, presumably, the other major eisosome structural components) has already reached a plateau (18,19). After cytokinesis, when the detached bud turns itself into a novel mother cell, eisosome biogenesis is again initiated toward the new growing bud. Thus, in contrast to growing buds, mother cells contain a population of already assembled eisosomes where the average Pil1-GFP intensity per eisosome remains invariant during a complete cell cycle. It has been previously proposed that, in mother cells, the already assembled eisosomes cores are static; that is, they do not actively exchange core subunits because Pil1-GFP fluorescence recovers very slowly after bleaching (17). However, similar fluorescence-recovery-after-photobleaching experiments performed at physiological temperature (30°C) suggest that, over a time period equivalent to one-half of a cell cycle (45 min), the mother cell's eisosomes exchange ~30% of their Pil1-GFP content (19). To gain a better understanding of the molecular dynamics of already assembled eisosomes, we decided to first characterize their core components in different compartments of mother cells.

For this, we used FCS analysis of temporal fluorescence intensity fluctuations to obtain both high-resolution data on molecular dynamics within a single illumination volume (point-scanning FCS) and positional information of different molecular dynamics (orbit-scanning FCS). Yeast strains bearing single-copy versions of C-terminally tagged Pil1 and Lsp1 driven by their native promoters and located in the natural genomic loci were scanned using a two-photon excitation fluorescence microscope equipped with a photon-counting detector. Point and circular scans were performed on different compartments of mother cells. The trajectory of the circular scans was chosen encompassing the cytoplasm, the plasma membrane, and eisosomes (Fig. 1 *A*).

Control point FCS and orbit-scanning FCS experiments on yeast cells with no fluorescent protein showed minimal autofluorescence and no correlations were detected. On the other hand, control-point FCS experiments with cytoplasmic monomeric Venus (mVenus) expressing cells

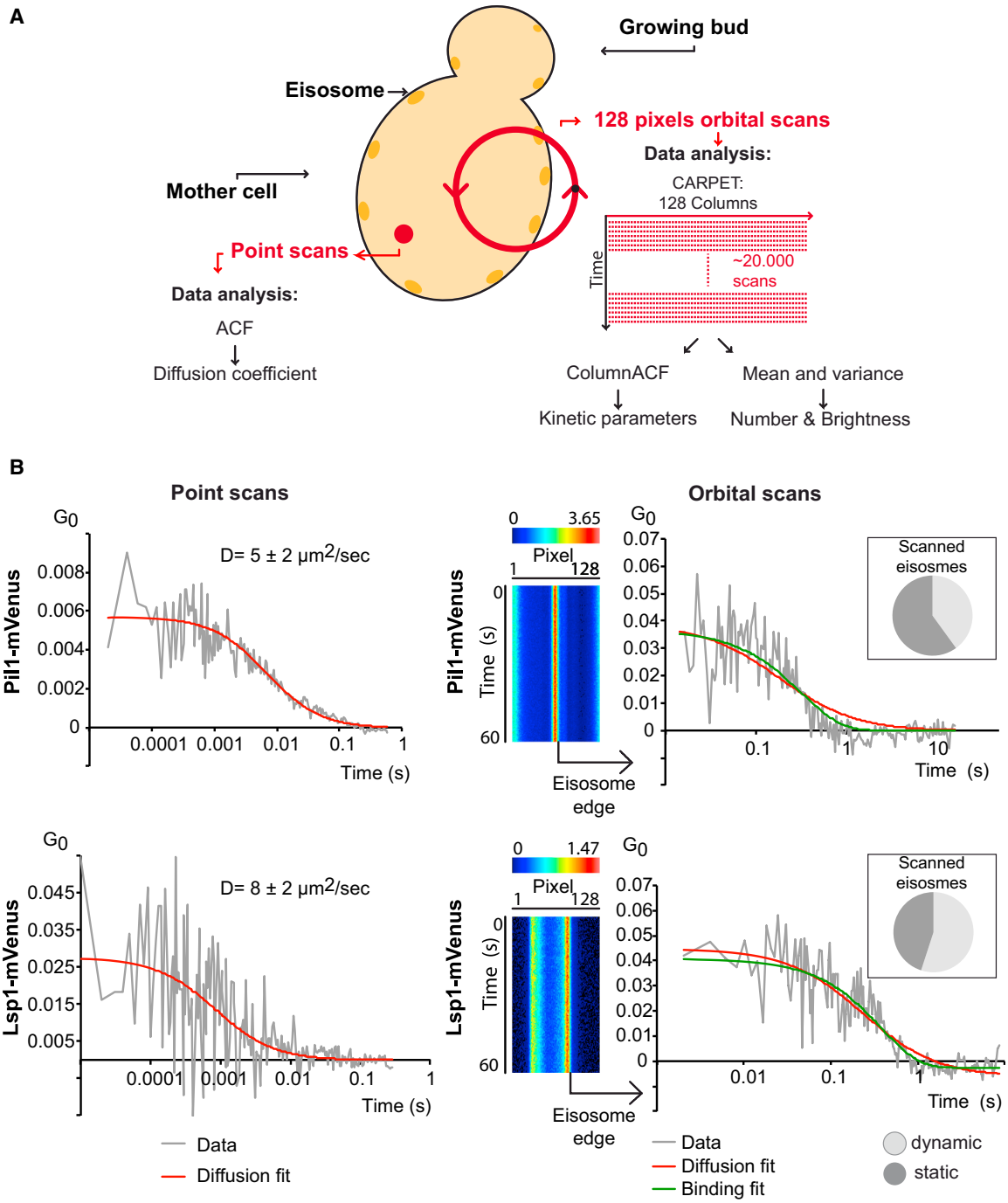

FIGURE 1 ACF analysis of Pil1 and Lsp1 at different subcellular locations. (*A*) Graphic representation of point- and circular-scans-based ACF analysis. Each yeast cell is focused at the equatorial plane and scanned by an immobile beam positioned at the cytoplasm (*point*) or by a circular orbit that passes through an eisosome. (*B*) (*Left panels*) Pil1 and Lsp1 exhibit cytoplasmic free diffusion dynamics. Representative ACF plots and free diffusion fittings of data coming from indicated yeast strains that were subjected to point scans at the cytoplasm. (*Right panels*) Circular scans reveal Pil1 and Lsp1 dynamic populations at the eisosome's edges. Representative fluorescence intensity carpets of Pil1-mVenus and Lsp1-mVenus cells are shown. ACF was calculated for each column/pixel of the carpet. When detected, autocorrelation data was plotted and fitting to free diffusion (*red*) and binding-unbinding equilibrium (*green*) models were tested. (*Insets*) Distribution of dynamic and nondynamic Pil1 and Lsp1 pools over a total of 25 and 20 individually scanned eisosomes, respectively. Parameter values (D_{app}, G_0, K, and A) and fitting statistics of analyzed cells are given in Table S1. To see this figure in color, go online.

evidenced autocorrelation yielding an apparent diffusion coefficient (D_{app}) of 11.2 ± 0.5 $\mu m^2/s$ (Fig. S1), which is consistent with the dynamic behavior of this protein in bacterial cells (24) and of similar fluorescent proteins located in the budding yeast's cytoplasm (25). Data obtained from cytoplasmic point scans of Pil1-mVenus cells were individually fit to a free diffusion model. After fitting analysis, we could determine that cytoplasmic Pil1-mVenus dynamic behavior is compatible with free diffusion exhibiting a D_{app} of 5 ± 2 $\mu m^2/s$ (Fig. 1 *B*, *top-left panel*). Equivalent imaging, processing, and analysis for Lsp1-mVenus cells indicated that, like Pil1-mVenus, the dynamic behavior of Lsp1-mVenus obeys free diffusive kinetics with a D_{app} of 8 ± 2 $\mu m^2/s$ (Fig. 1 *B*, *bottom-left panel*).

A subset of eisosomes exhibits binding-unbinding Pil1 and Lsp1 dynamics

Overall, these results show that cytoplasmic Pil1 and Lsp1 pools behave as relatively free diffusing molecules with D_{app} that are compatible with low aggregation states (monomeric to oligomeric). Point-FCS provides dynamic information at a single spatial location and turned out to be inadequate to obtain meaningful data when sampling at eisosome cores or eisosome edges was attempted. To address the dynamic behavior of Pil1 and Lsp1 we employed orbital scans, which enabled us to simultaneously evaluate different cellular locations (Fig. 1 *A*). Orbital scans have sampling interval times much longer than those used for point-FCS sampling. Although this sampling frequency is too slow to detect free diffusing monomeric molecules like mVenus, it allowed us to detect slower moving particles, which is something we can expect from plasma membrane proteins and/or large complexes within the cytoplasm. To simplify the analysis visualization, the intensity data captured by the scanning orbit is displayed in two-dimensional carpets where the *x* dimension corresponds to each orbit pixel and the *y* dimension corresponds to time (Fig. 1 *B*, *right panels*). Autocorrelation analysis for each point in the orbit (the columns in the carpet) was performed for >20 Pil1-mVenus and >25 Lsp1-mVenus cells registered over three independent experiments. This analysis enabled us to identify a common pattern: autocorrelation was detected in pixels located at the edges of eisosomes and not within them (Fig. 1, *right panel*). Fitting of the autocorrelation function (ACF) was done using a free diffusion null hypothesis model, but results indicated that this model was not fitting the data well. The deficient fittings to a free diffusion model of the ACFs of moving particles located at the eisosomes edges were characterized by a narrowing of the ACFs with respect to the model (see examples for Pil1 and Lsp1 in Fig. 1 *B*). In contrast, all diffusion models, regardless of whether they represent normal, hindered, or anomalous diffusion, will produce a broader ACF. Instead, we have observed a narrowing of the ACF, which is typical of binding equilibrium. Consistently with this hypothesis, an ACF exponential formula characteristic of binding-unbinding equilibrium to an immobile fraction (the eisosome core) provided a better fit in the totality of pixels analyzed, giving mean first-order kinetic constants of 2.9 ± 0.6 s^{-1} for Pil1-mVenus and 3.1 ± 0.9 s^{-1} for Lsp1-mVenus (Table S1).

These results suggest that, within mother cells, both Pil1 and Lsp1 partition in at least three dynamically different populations: 1) an immobile fraction at the eisosome's core, 2) a cytoplasmic free-diffusing fraction with D_{app} compatible with monomeric or low aggregation states, and 3) an eisosome-associated fraction that is dominated by a binding-unbinding equilibrium behavior and localizes at the eisosomes edges. Remarkably, the eisosome-associated dynamic fraction detected at some eisosomes was absent in other eisosomes of cells that were similarly grown and scanned. Orbital-scan measurements and ACF analysis showed that the eisosome-associated Pil1 and Lsp1 dynamic populations were present in 40 and 55% of individually scanned eisosomes, respectively (see Fig. 1 *B*, *insets*, *right panels*). Moreover, for both proteins, these mobile fractions were always detected at the eisosome edges and not at the eisosomes cores. Thus, our results indicate that a subset of mother cell eisosomes is static whereas there is another fraction of eisosomes with boundaries containing dynamic pools of Pil1 and Lsp1.

Number and brightness analysis reveals the aggregation states of the different eisosome core proteins' subcellular pools

Diffusion coefficient values obtained by ACF analysis suggest that cytoplasmic Pil1 and Lsp1 exist as either monomeric or low aggregation states. Moreover, whether the eisosome-associated Pil1 and Lsp1 dynamic pools are either monomeric or preassembled is also uncertain. To address these points, we obtained a cellular map of Pil1 and Lsp1 aggregation states performing N&B analysis over the same temporal intensity fluctuations data analyzed by ACF. N&B is based on moment-analysis that utilizes the average intensity and the variance in the intensity distribution at each pixel to calculate the number (N) of diffusing particles within the illumination volume and their apparent brightness (B) (26). In the simplest case, the molecular brightness ε (where $\varepsilon = B-1$) of an n-mer oligomer is n times the monomer brightness. Thus, providing a pixel-by-pixel map of number and brightness in an image, N&B analysis enables us to determine the oligomerization state/s of proteins in living cells with high spatial resolution (see the Supporting Material for a more detailed description).

Intensity fluctuations data of mVenus-bearing cells were used as the reference of the brightness of the monomeric

fluorophore. Because we used a yeast strain that expresses mVenus from a multicopy plasmid and because the number of copies per genome of this type of expression vectors varies from cell to cell (27), the resulting population of mVenus cells has a wide distribution of mVenus intensities. This cell-to-cell variation in mVenus expression levels enabled us to determine that our brightness calculations were robust over a wide range of fluorescence intensities. Within each experimental set, mVenus brightness histograms were fitted to Gaussian distributions and used to calculate the average monomeric brightness value (Fig. 2 *A*). Pil1-mVenus brightness histograms exhibited a predominant population similar to mVenus and a minor population corresponding to higher brightness values (Fig. 2 *A*). Visual inspection of intensity and brightness values in the expanded orbits carpets, where the *x* dimension corresponds to each orbit pixel and the *y* dimension corresponds to independent measurements, suggested that the cytoplasm is mainly occupied by Pil1-mVenus with the brightness values similar to mVenus whereas higher brightness populations are found at eisosome's edges (Fig. 2 *B*). Similar brightness populations were detected for Lsp1-mVenus (data not shown). On the other hand, the eisosome core immobile fraction displays monomeric brightness values, which were more likely to have originated from fluctuations of the cytosolic pool.

To quantitatively assert the subcellular distribution of the different oligomeric populations, we segmented the orbit scans in three subcellular compartments (cytoplasm, eisosome core, and eisosome plus edges) using the intensity profile of the carpet (Fig. 3 *A*). Then, we classified brightness values in three categories: monomers, oligomers, and multimers, taking mVenus brightness values as a reference (see Fig. 3 *B* and the Supporting Material). The statistical analysis represented as overlapped box and dot plots confirms what is observed in Fig. 2 *B*: in wild-type cells, only 8% of Pil1-mVenus corresponds to oligomers, and multimers are few. Moreover, this analysis reinforces the hypothesis that eisosome edges are populated by a dynamic oligomeric fraction of Pil1, as has already been shown in Fig. 2 *B*. Considering all these results, we interpret the presence of Pil1 oligomers as a dynamic subpopulation that binds and dissociates from eisosomes with a kinetic constant of $2.9 \pm 0.6\ s^{-1}$ (Figs. 1, 2, and 3 and Table S1). We note that fluctuations at both edges of the same eisosome are uncorrelated, ruling out that eisosome movements, as a whole, are responsible for the fluctuations at the eisosomes' edges.

Number and brightness plots provide the opportunity to determine the averaged distance between oligomers and the eisosome core. For this, we selected the number and brightness profiles of all the eisosomes with detected oligomers and fitted N&B profiles to Gaussian distributions (Fig. S2). Mapping of the centers of mass of the resulting Gaussian fits indicated that the mean distance between oligomers and eisosomes is 275 ± 60 nm, a value that resides within the dimensions of eisosomes (200–400-nm long and 50-nm deep). We asked whether this oligomeric population of Pil1 is sensitive to protein concentration. To address this point, we analyzed cells in which a high-copy vector containing *PIL1-mVENUS* was the sole source of Pil1 (see Materials and Methods for more details). Overexpression of Pil1 produces a normal number of eisosomes per cell, but with higher content of Pil1 per eisosome (18). N&B analysis of *PIL1*-overexpressing cells showed that, indeed, an increase in Pil1 protein concentration correlates with the appearance of higher amounts of oligomers and even higher-order assemblies (Figs. S3 and 3 *B*). Quantitative analysis of the cytoplasm fluorescence average intensity and brightness of overexpressed Pil1-mVenus showed that the artificial increment of cytoplasm protein concentration leads to the generation of bigger oligomeric and even multimeric aggregates of Pil1-mVenus within the cytoplasm (Fig. S3 *C*).

Fluorescence lifetime quenching analysis demonstrates that Pil1 and Lsp1 directly interact in the cytoplasm and at eisosomes

Our results indicate that Pil1 and Lsp1 coexist in the cytoplasm of mother cells sharing similar D_{app} (Fig. 1). Immunoprecipitation of whole-cell extracts followed by mass spectrometry analysis shows that both proteins physically interact in a close to equimolar relationship (17). In vitro, both proteins Pil1 and Lsp1 are able to form homodimers and high-order macromolecular assemblies (19–21). Despite all this evidence, it is still unknown whether the eisosome core proteins interact directly in live cells.

To address this point, we first asked whether *LSP1* deletion changes Pil1's cytoplasmic aggregation state. Previously, it has been shown that in the absence of Lsp1, there is a slight decrease in the number of eisosomes per cell (0.7-fold) and moderate increases in Pil1-GFP cytoplasmic and eisosome contents (1.8-fold and 1.7-fold, respectively), indicating that Pil1 by itself is still able to form wild-type-like eisosomes (17,18,22). Regardless of the mild phenotype of eisosomes' organization showed by *lsp1*Δ cells, N&B analysis of Pil1-mVenus revealed a more specific phenotype (Fig. S4). When compared with wild-type cells, N&B maps and box plots of *lsp1*Δ cells showed an overall increase in Pil1-mVenus brightness values. This increase is evident at eisosome edges and it is also detected within the cytoplasm (Fig. S4). These results, indicating that the lack of Lsp1 leads to an increase in the cellular content of Pil1 with higher brightness values, suggest that Pil1 homo-aggregation replaces Pil1-Lsp1 heterodimers that normally exist in wild-type cells.

To challenge this hypothesis, we performed Förster resonance energy transfer (FRET) experiments between Pil1 and

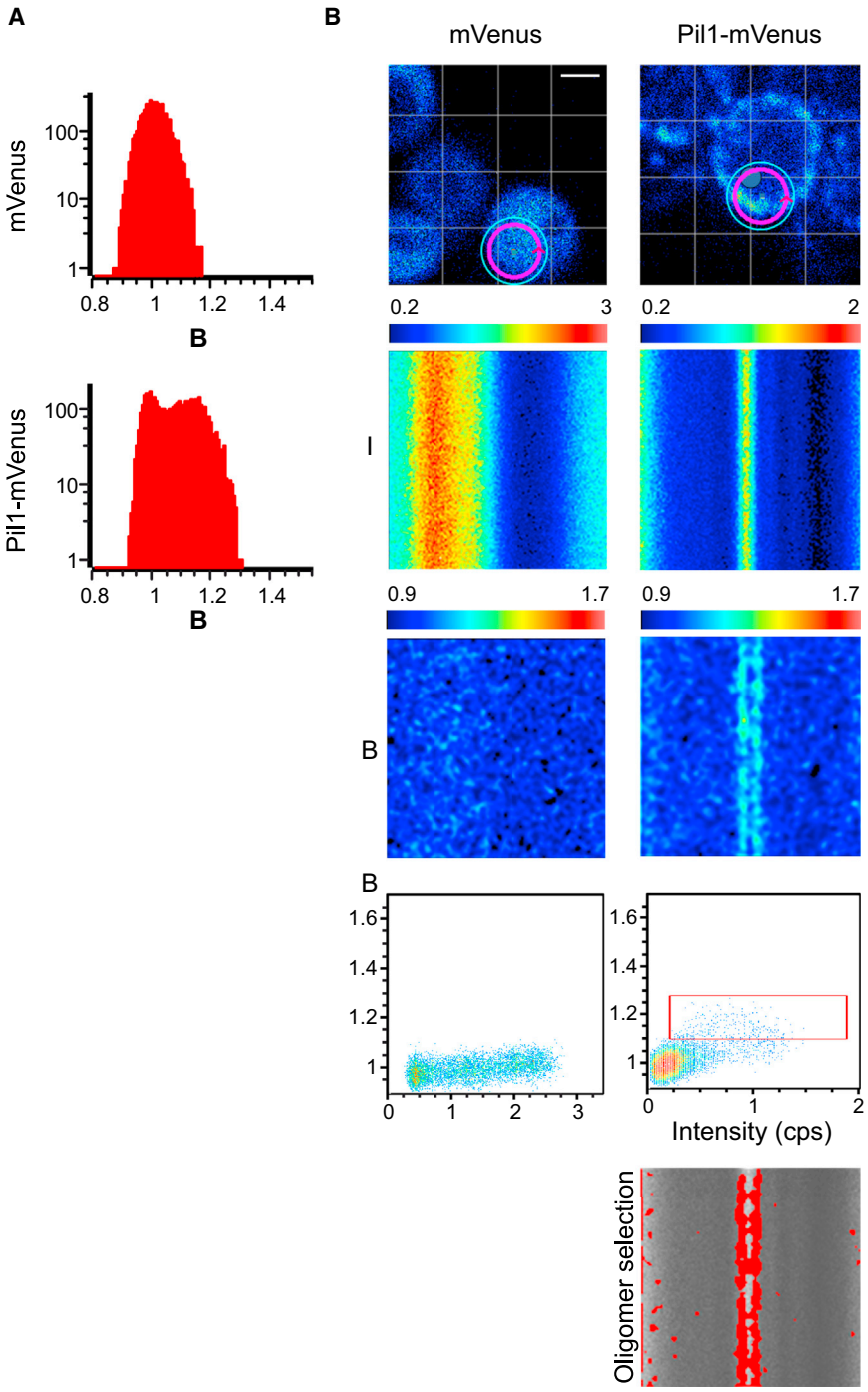

FIGURE 2 Pil1 presents different oligomer states depending on its subcellular localization. Yeast strains carrying either mVenus or Pil1-mVenus were subjected to circular scans and N&B analysis. (*A*) Apparent brightness histograms of one representative cell. (*B*) First-row panels show representative images of cells scanned with circular orbits (*magenta circular line*; *arrowhead*, scan starting point). The second- and third-row panels display corresponding carpets with intensity (*I*) and brightness (*B*) values. Each carpet is composed of 128 columns representing each pixel of the orbit and 128 rows, each one corresponding to an independent set of measurements (see the Supporting Material for more detail). Intensity carpet for Pil1-mVenus cell presents two eisosomes with cores at columns 1–4 and 59–63. Fourth-row panels show brightness- versus intensity-plots; (*red box*) selected pixels with brightness values higher than monomeric mVenus (for a more detailed explanation of oligomer selection, see the Supporting Material). These pixels are false-colored (*red*) in the grayscale B-carpets (*bottom panel*). Scale bar: 2 μm. To see this figure in color, go online.

Lsp1 using both possible combinations of donor- (mVenus) and acceptor- (mCerulean) tagged proteins in live cells. To detect FRET and to measure its efficiency, we used the donor's lifetime quenching as the readable output. Fluorescence-lifetime-imaging microscopy (FLIM) measurements were performed by image acquisition in the frequency domain and represented using the phasor approach (28). In this approach, the donor's fluorescence lifetime in each pixel of the FLIM raster scan is represented in a two-dimensional polar plot (the phasor plot). In the case of FRET, quenching of the donor's fluorescence lifetime is evidenced by displacement of the lifetime pixel population within the phasor plot (Fig. 4 *A*). Thus, comparison of donor-only with donor-acceptor phasor plots allows the detection of shifts in lifetime pixel populations due to FRET. Moreover, quantitative evaluation of FRET efficiencies (Table 1) can be performed without fitting to exponential models (28,29). Phasor plots representing the totality of cellular

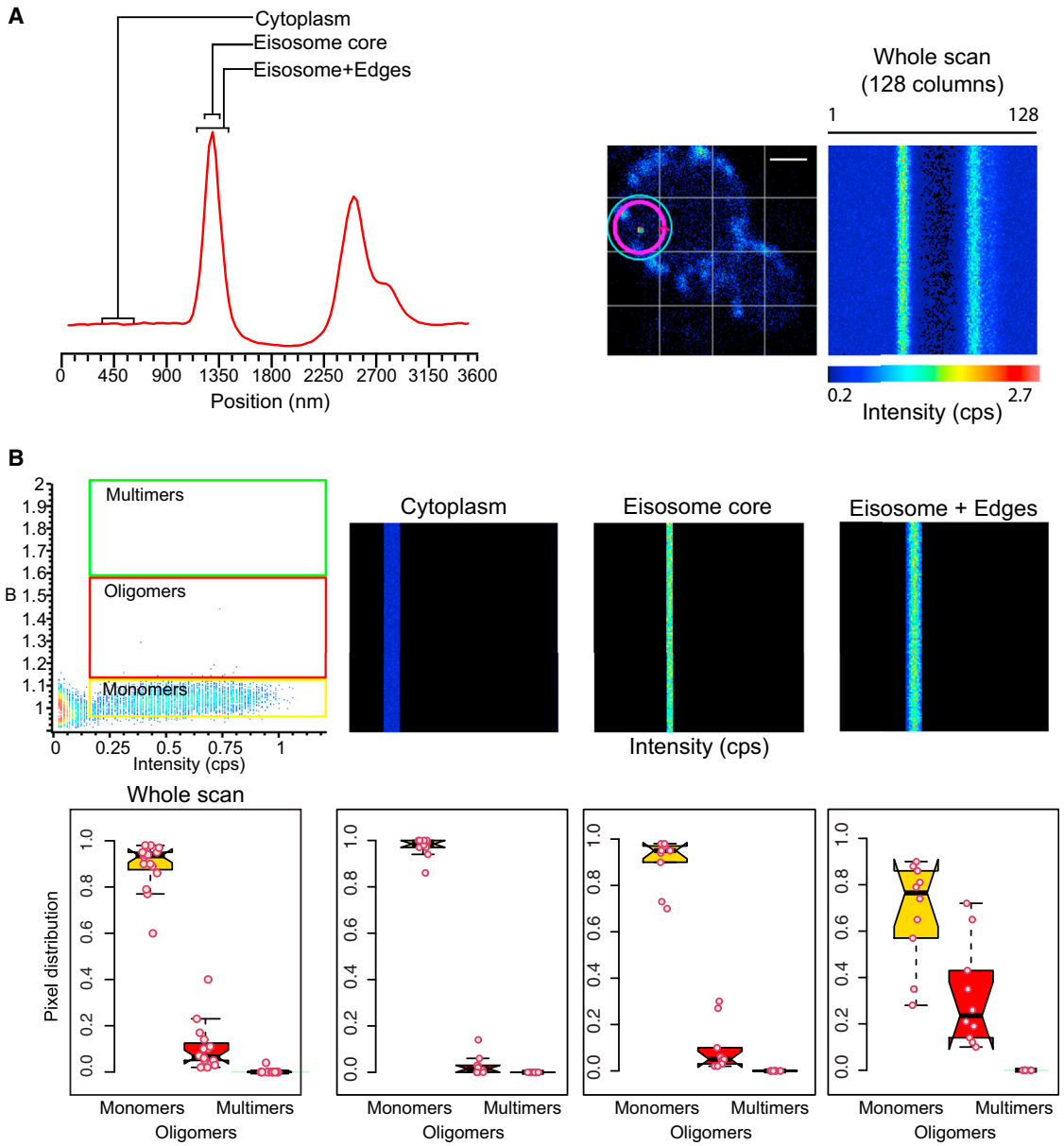

FIGURE 3 Pil1 aggregation states subcellular quantitation. (*A*) Subcellular compartments definition criteria. (*Red*) Intensity profile of a 128-pixel circular scan of a Pil1-mVenus yeast cell. Eisosome core consists of a 212-nm-wide area encompassing the intensity center of mass. Eisosome edges are defined as the eisosome core's contiguous 159-nm-wide areas and the cytoplasmic compartment is defined as the central 530-nm-wide area of cytoplasmic signal (for a more detailed explanation, see the Supporting Material). Scale bar: 2 μm. (*B*) Monomeric, oligomeric, and multimeric ranges of brightness values were defined in relation to mVenus brightness-value distributions (for a more detailed explanation, see the Supporting Material). Intensity value (I-) carpets for each subcellular compartment as defined in (*A*) are shown. Boxplots show the statistical analysis of the pixel distribution belonging to each species in the whole scan and within each subcellular compartment as defined in (*A*). Data from three independent experiments with at least six cells per experiment were analyzed. To see this figure in color, go online.

pixels showed a clear decay in the donor lifetime, indicating that Pil1 and Lsp1 directly interact in vivo (Fig. 4 *A*, *two left panels*). To identify the subcellular source/s of the FRET signal we filtered the pixels into cytoplasm, eisosomes, and eisosome edge compartments (Fig. 4 *B*). In all cases, filtered pixels were displaced toward lower lifetime values, indicating that Pil1-Lsp1 direct interaction occurs in all subcellular compartments (Fig. 4 *C*, *two left panels*).

This result was independent of the protein donor carrier protein and, moreover, we observed higher FRET efficiency when the mCerulean carrier was Lsp1 (Fig. 4 *C* and Table 1). Considering unquenched mCerulean lifetimes in donor-only strains and autofluorescence, we calculated the FRET efficiencies for the donor-acceptor strains (see the Supporting Material for details). Table 1 summarizes the different FRET efficiencies for the complete set of

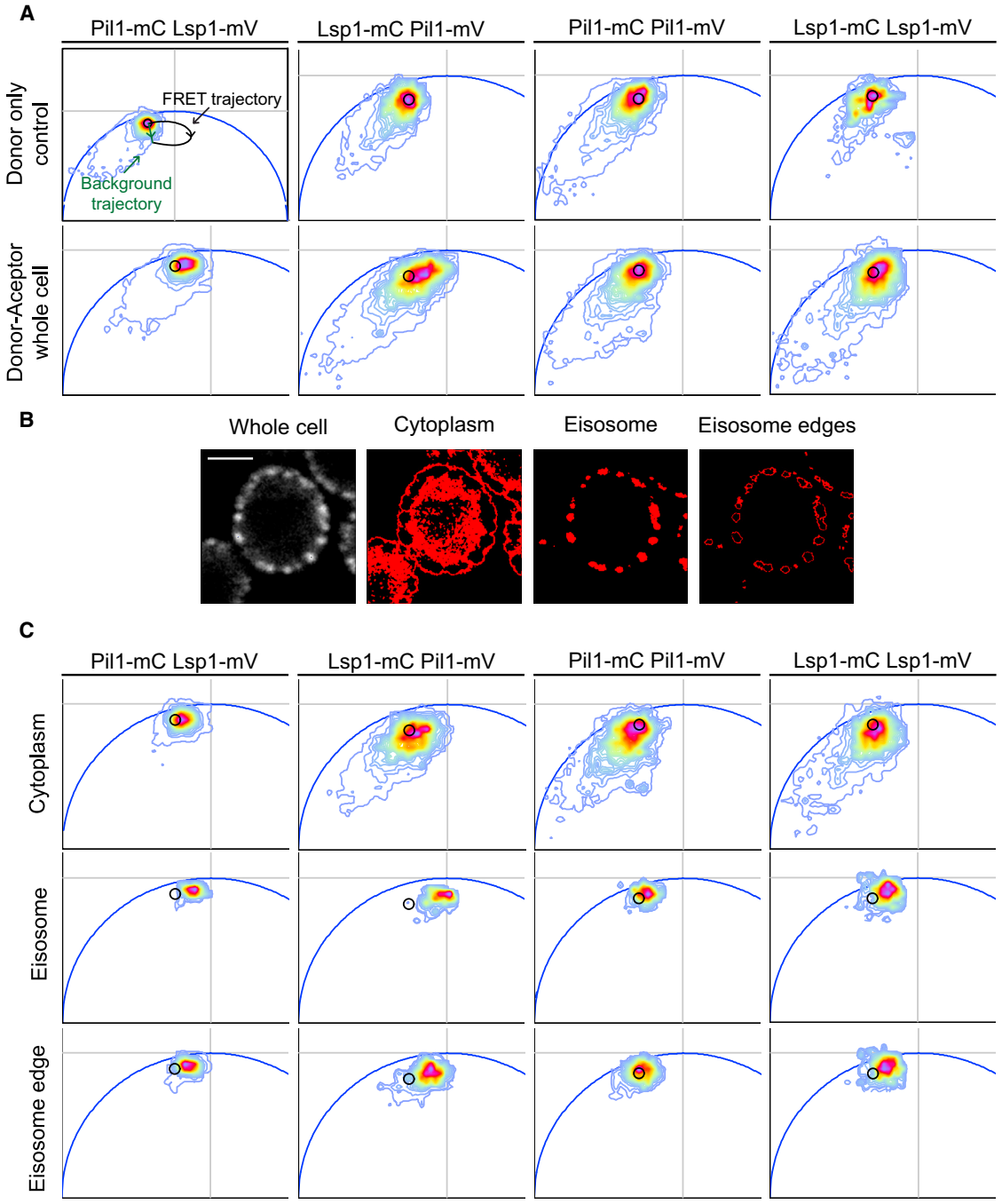

FIGURE 4 FLIM-FRET analysis of Pil1 and Lsp1 direct interactions in vivo. All possible combinations of mCerulean- and mVenus-tagged Pil1 and Lsp1 strains were imaged with a two-photon microscope equipped with a FLIMbox (ISS, Champaign, IL) and results were analyzed using the phasor plot approach. (*A*) Phasor distribution of lifetimes measured in cells expressing the fluorescent donor-only controls (Pil1-mCerulean or Lsp1-mCerulean) or donor-acceptor pairs. A theoretical FRET trajectory (*black curved arrow*) and a background trajectory (*green arrow*) are shown within the Pil1-mCerulean donor-only phasor plot (*upper-left*). The trajectory originates at the black circle (which represents 0% FRET efficiency), whereas the trajectory's end corresponds to 100% FRET efficiency. The black circle is concentric to the donor-only pixel distribution center-of-mass, and encompasses 80% of the pixels. This circle is repeated in phasor plots above as a visual reference of the donor-only center-of-mass position. (*B*) Example of fluorescence-intensity-based subcellular compartments segmentation. Scale bar, 2 μm. (*C*) Phasor plots of pixels' lifetimes corresponding to the subcellular compartments as defined in (*B*). All phasor plots presented with pixel distribution lifetimes were built from the integration of six or more cells in each plot. From violet until red color, one standard deviation of the pixel dispersion is comprehended, and two standard deviations are contained until yellow. Phasor plots are shown zoomed-in for better visualization. To see this figure in color, go online.

TABLE 1 FRET efficiencies

Strain	Whole cell	Eisosome	Eisosome edge	Cytoplasm
Pil1-mC Lsp1mV	5	10	10	5
Lsp1mC-Pil1mV	12	20	17	12
Lsp1-mC Lsp1-mV	20	30	20	0
Pil1-mC Pil1-mV	10	20	15	0
Pil1-mC Pil1-mV *lsp1*Δ	5	28	18	10

Yeast strains expressing the different possible donor-acceptor FRET pairs were imaged for fluorescence lifetime data acquisition (see the Supporting Material for detail). For each strain, pixel distribution lifetimes coming from at least six different cells were integrated within the same phasor plot. FRET trajectories in the phasor plots were calculated and, for each subcellular segmentation, the FRET efficiency of the center of mass of pixel distribution in the phasor plot was calculated using the FRET calculator of SIMFCS (Globals Software, Laboratory for Fluorescence Dynamics, http://www.lfd.uci.edu/globals/). See Figs. 4 and S5 for visual inspection of phasor plots for center-of-mass positions and pixel population dispersions.

analyzed cells, discriminating among the different subcellular regions.

Thus, our point-FCS (Fig. 1), N&B (Figs. 2 and 3), and FLIM-FRET results strongly suggest that the cytoplasm of wild-type cells is populated by Pil1-Lsp1 heterodimers. However, these findings do not rule out the existence of a more complex scenario where Pil1-Pil1 and/or Lsp1-Lsp1 homodimers also contribute to eisosome structure. To address this possibility, we constructed heterozygote diploid strains containing either Pil1-mCerulean/Pil1-mVenus or Lsp1-mCerulean/Lsp1-mVenus pairs (Table S2) and performed live FLIM-FRET experiments. Phasor plots of the whole cellular signal showed decreases in the donor lifetime in Lsp1-Lsp1 pairs (Fig. 4 *A*, *right panel*) and, to a lesser extent, in Pil1-Pil1 pairs as well (Fig. 4 *A*, *third panel*). Phasor plot of the different subcellular compartments showed a donor lifetime reduction in eisosome and eisosome-edge pixels, but not in cytoplasmic pixels (Fig. 4 *C*, *right panels*). Calculated FRET efficiencies for both homo pairs across different cellular compartments confirm the lack of homotypic interaction in the cytoplasm and the presence of Pil1-Pil1 and Lsp1-Lsp1 interactions at eisosomes and eisosome edges (Table 1). We interpret the existence of homotypic interactions to be a result of higher-order assembly of Pil1-Lsp1 heterodimers at eisosomes and eisosomes' edges.

DISCUSSION

Using a complementary set of fluorescence fluctuation analysis methods, we have systematically addressed the dynamic properties of eisosome core proteins Pil1 and Lsp1 in live cells. In a simplistic view, eisosome assembly occurs in daughter cells (growing buds), whereas, in mother cells, already-assembled eisosomes are in a steady state. In this work, we focused on Pil1 and Lsp1 behavior within the cytoplasm and eisosome compartments of mother cells. Further work will be directed toward the understanding of eisosome assembly in daughter cells.

Based on several examples of our experimental evidence, we propose that the Pil1-Lsp1 heterodimer constitutes the eisosome's minimal building block, as follows. First, Pil1-mVenus (molecular mass 65.8 kDa) and Lsp1-mVenus (molecular mass 65.5 kDa) cytoplasmic populations exhibit D_{app} (5 ± 2 $\mu m^2/s$ and 8 ± 2 $\mu m^2/s$, respectively) that, when compared with mVenus (molecular mass 27.5 kDa, $D_{app} = 11 \pm 0.2$ $\mu m^2/s$), are compatible with dimeric or low aggregation states (Fig. 1). Second, live FLIM-FRET results indicate Pil1 and Lsp1 directly interact in the cytoplasm and eisosomes (Fig. 4 and Table 1). Third, similar FLIM-FRET experiments detected Pil1-Pil1 and Lsp1-Lsp1 homotypic interactions only where assembled scaffolds and oligomers are present (Fig. 4 and Table 1). Because the Pil1-Pil1 donor-acceptor pair does exhibit positive FRET signals at cytoplasmic pixels in *lsp1*Δ cells (Fig. S5 and Table 1), we reason that negative FLIM-FRET results for Pil1-Pil1 cytoplasmic homotypic interaction in wild-type cells cannot be attributed to insufficient closeness and/or orientation of the donor and acceptor dipoles. Fourth, N&B analysis of Pil1-mVenus and Lsp1-mVenus in wild-type cells detected cytoplasmic brightness values equivalent to mVenus only (Figs. 2 and 3, and data not shown). Although we cannot rule out the possibility that a fraction of cytosolic Pil1 and/or Lsp1 may exist in a monomeric state, the cytoplasmic dominance of monomeric brightness values for both proteins is better interpreted as arising from Pil1-Lsp1 heterodimers. Based on ACF and N&B analysis, we calculate the concentration of Pil1-Lsp1 cytoplasmic heterodimers to be ~400–800 nM. Thus, our results suggest that the cytoplasm of mother cells contain mainly Pil1-Lsp1 heterodimers in the nanomolar concentration range. Both point and orbital scans were applied to mother cells carrying small- to mid-size buds, and therefore, our estimations integrate cells that transit the G2/M phase. This is relevant in the context of eisosome biogenesis, which is cell-cycle-regulated and occurs in correlation with a burst of Pil1 total protein levels during G2/M phase (18). However, as of this writing, whether Pil1-Lsp1 cytoplasmic heterodimers levels fluctuate during the cell cycle, and growing buds are occupied by similar Pil1-Lsp1 cytoplasmic species and concentrations, is unknown.

Although orbital scans were performed over a wide range of sampling intervals (488–122 Hz), we were unable to detect autocorrelation of fluorescence fluctuations at eisosome cores. However, the presence of Pil1 and Lsp1 mobile fractions immediately located next to eisosome highest-intensity pixel values indicates that already-built eisosomes are not completely static assemblies, but instead exhibit heterogeneous dynamics. ACF analysis suggests that both Pil1 and Lsp1 eisosome-associated mobile fractions follow first-order binding-unbinding kinetics with similar rate constants (Fig. 1). Brightness values indicate the existence of similar

aggregation states for both proteins, and FLIM-FRET results indicate that Pil1 and Lsp1 directly interact at eisosomes borders, where oligomers are located (Fig. 4). Taken altogether, our results support the idea that the independently observed Pil1 and Lsp1 oligomers belong to the same dynamic entity.

Which is the subcellular compartment where Pil1-Lsp1 oligomers partition? As of this writing, whether it is the plasma membrane or the cytoplasm is unknown. Because oligomers are not detected further away from eisosomes, it seems unlikely that they partition within the cytoplasm. Quantification of the most probable distances between the eisosomes' centers of mass and oligomers give values within the range of eisosome dimensions. Because of the comparable dimensions of the point-spread function (PSF) of our scanning system (300-nm axial diameter) and eisosome dimensions, we acknowledge that eisosomes can be encompassed by a single PSF. However, Gaussian fits for N&B distributions locate brightness centers away from eisosome centers of mass within a distance that is comparable with PSF axial diameter (Fig. S2). Therefore, we propose that oligomers are located at or near to eisosome edges. Taken together, the binding-equilibrium-dominated kinetics and the short-range location area suggest that oligomers are plasma-membrane-bound entities. In this view, steady-state eisosomes exchange Pil1-Lsp1 oligomeric subunits composed by Pil1-Lsp1 heterodimers that are still attached to the plasma membrane. Either total-internal-reflection-fluorescence microscopy coupled to ACF analysis or super-resolution live imaging techniques compatible with single-particle tracking should help to clarify this issue.

Remarkably, orbital scans, ACF, and N&B analysis of eisosomes with similar intensity profiles show that not all, but a subset, contains dynamic Pil1-mVenus and Lsp1-mVenus oligomers (Fig. 1 *B*, *right panel insets*). Thus, we can distinguish at least two different populations of mother cells' eisosomes: one where the main structural proteins remain static, and one where what we call an "active population" is being remodeled (and which is evidenced by the presence of mobile oligomers). This can explain why different fluorescence-recovery-after-photobleaching experiment analyses alternatively reported zero recovery and small but significant recovery of Pil1-GFP fluorescence after photobleaching (17,19). Because our measurements provide a local snapshot of the complete cell, we do not know whether active eisosomes remain as such, or if they switch to an alternative state with no structural proteins exchange.

An attractive speculation is that these two eisosome populations reflect the dynamic partition within the plasma membrane of different cellular events. Consistent with this idea, work on Slm1 and Slm2 indicates that these signaling proteins, which mediate TORC2-dependent control of lipid homeostasis, colocalize with a subset of eisosomes. Moreover, this discrete localization pattern is dynamic and responds to plasma membrane stress caused by membrane stretch or sphingolipids synthesis inhibition (16). Pil1 and Lsp1 are multiphosphorylated proteins, and their phosphorylation status depends on the activities of the Pkh1/2-Ypk1/2 and Pkc1 kinases' signaling pathways (13,30,31). Pkh2 concentrates in plasma membrane foci that are restricted to a subset of eisosomes (22). *PKH2* (and also *PKH1*) overexpression leads to Pil1 and Lsp1 hyperphosphorylation and to eisosomes disassembly (14). It is proposed that hyperphosphorylation of Pil1 and Lsp1 obliterates the capacity of positively charged residues to interact with the plasma membrane. Pil1 and Lsp1 membrane binding depends in part on positively charged residues that interact with phosphatidylinositol (4,5)-biphosphate (PI(4,5)P2), and are located within their BAR domains (21). PI(4,5)P2 depletion, like Pkh kinases overexpression, leads to eisosome disassembly strongly suggesting that protein-lipid electrostatic interactions are paramount to maintain eisosome core proteins cohesion within the plasma membrane (21). It has been previously demonstrated that eisosomes are needed for PI(4,5)P2 phosphatases Inp51 and Inp52 recruitment to the plasma membrane (32).

It has been recently demonstrated that the PI(4,5)P2 phosphatase Inp51 is recruited within a subset of eisosomes (33). Taking all these observations together, it seems evident that eisosomes are not homogeneous regarding different signaling molecules' recruitment. Thus, it is tempting to speculate that active eisosomes might be sites where either Inp51 and/or Pkh2 concentrate and therefore modify the plasma membrane composition and/or structural proteins leading to eisosome remodeling. Although there is no evidence showing that active eisosomes are the sites where signaling molecules such as Slm1/2 and Pkh2 transiently concentrate, these separate observations still argue in favor of the specialization of eisosomes as sites of specific signaling events.

This study highlights the value of combined fluorescence fluctuation analysis methods in defining the dynamics of eisosomes and their constitutive proteins. Much as single-cell experiments have begun to reveal many novel aspects of cell-to-cell variation, our single-eisosome analysis underlines the capacity of FCS methods to interrogate functional diversity within apparently homogeneous subcellular structures. Further work combining these methodologies and others related, such as super-resolution- and total-internal-reflection-fluorescence-FCS, will be crucial to uncover functional relationships between eisosomes and the different signaling pathways that dynamically locate within.

SUPPORTING MATERIAL

Supporting Materials and Methods, six figures and two tables are available at http://www.biophysj.org/biophysj/supplemental/S0006-3495(15)00171-X.

AUTHOR CONTRIBUTIONS

A.O.-C. performed all the experiments described in the study with help from V.S. (strains construction) and M.M. (strains verification). A.O.-C. processed and analyzed the data with input from E.G., P.S.A., and M.A.D. P.S.A. and A.O.-C. conceived the project, guided the experiments, and wrote the article with input from E.G.

ACKNOWLEDGMENTS

We thank Alejandro Colman-Lerner for reagents, Alessandro Rossetta for helpful advice in data processing, and Laura Estrada Leonel Malacrida, and members of the Gratton and Aguilar laboratories for scientific advice and comments on the article.

This work was supported by the Agencia Nacional de Investigación e Innovación de Uruguay (grant No. FCE-3-2011-1-5942 and Travel Fellowship to P.S.A. and A.O.-C.), the Programa de Desarrollo de Ciencias Básicas, the MERCOSUR Structural Convergence Fund (Fondo para la Convergencia Estructural del MERCOSUR, FOCEM, COF 03/11), the National Institutes of Health (grants No. NIH P41-GM103540 and No. NIH P50-GM076516 to E.G. and M.A.D.), the Journal of Cell Science Traveling Fellowship (to A.O.-C.), a Wood/Whelan Fellowship from the International Union of Biochemistry and Molecular Biology (to A.O.-C.), and Master and Doctoral fellowships from Sistema Nacional de Becas (to M.M. and A.O.-C., respectively).

SUPPORTING CITATIONS

References (34–37) appear in the Supporting Material.

REFERENCES

1. Matsumoto, K., J. Kusaka, …, H. Hara. 2006. Lipid domains in bacterial membranes. *Mol. Microbiol.* 61:1110–1117.
2. Simons, K., and J. L. Sampaio. 2011. Membrane organization and lipid rafts. *Cold Spring Harb. Perspect. Biol.* 3:a004697.
3. Tanos, B., and E. Rodriguez-Boulan. 2008. The epithelial polarity program: machineries involved and their hijacking by cancer. *Oncogene.* 27:6939–6957.
4. Kusumi, A., K. G. Suzuki, …, T. K. Fujiwara. 2011. Hierarchical mesoscale domain organization of the plasma membrane. *Trends Biochem. Sci.* 36:604–615.
5. Eggeling, C., C. Ringemann, …, S. W. Hell. 2009. Direct observation of the nanoscale dynamics of membrane lipids in a living cell. *Nature.* 457:1159–1162.
6. Bagatolli, L. A., and O. G. Mouritsen. 2013. Is the fluid mosaic (and the accompanying raft hypothesis) a suitable model to describe fundamental features of biological membranes? What may be missing? *Front. Plant Sci.* 4:457.
7. Olivera-Couto, A., and P. S. Aguilar. 2012. Eisosomes and plasma membrane organization. *Mol. Genet. Genomics.* 287:607–620.
8. Spira, F., N. S. Mueller, …, R. Wedlich-Söldner. 2012. Patchwork organization of the yeast plasma membrane into numerous coexisting domains. *Nat. Cell Biol.* 14:640–648.
9. Strádalová, V., W. Stahlschmidt, …, J. Malinsky. 2009. Furrow-like invaginations of the yeast plasma membrane correspond to membrane compartment of Can1. *J. Cell Sci.* 122:2887–2894.
10. Moor, H., and K. Mühlethaler. 1963. Fine structure in frozen-etched yeast cells. *J. Cell Biol.* 17:609–628.
11. Malínská, K., J. Malínský, …, W. Tanner. 2003. Visualization of protein compartmentation within the plasma membrane of living yeast cells. *Mol. Biol. Cell.* 14:4427–4436.
12. Grossmann, G., M. Opekarová, …, W. Tanner. 2007. Membrane potential governs lateral segregation of plasma membrane proteins and lipids in yeast. *EMBO J.* 26:1–8.
13. Zhang, X., R. L. Lester, and R. C. Dickson. 2004. Pil1p and Lsp1p negatively regulate the 3-phosphoinositide-dependent protein kinase-like kinase Pkh1p and downstream signaling pathways Pkc1p and Ypk1p. *J. Biol. Chem.* 279:22030–22038.
14. Walther, T. C., P. S. Aguilar, …, P. Walter. 2007. Pkh-kinases control eisosome assembly and organization. *EMBO J.* 26:4946–4955.
15. Grossmann, G., J. Malinsky, …, W. Tanner. 2008. Plasma membrane microdomains regulate turnover of transport proteins in yeast. *J. Cell Biol.* 183:1075–1088.
16. Berchtold, D., M. Piccolis, …, R. Loewith. 2012. Plasma membrane stress induces relocalization of Slm proteins and activation of TORC2 to promote sphingolipid synthesis. *Nat. Cell Biol.* 14:542–547.
17. Walther, T. C., J. H. Brickner, …, P. Walter. 2006. Eisosomes mark static sites of endocytosis. *Nature.* 439:998–1003.
18. Moreira, K. E., T. C. Walther, …, P. Walter. 2009. Pil1 controls eisosome biogenesis. *Mol. Biol. Cell.* 20:809–818.
19. Olivera-Couto, A., M. Graña, …, P. S. Aguilar. 2011. The eisosome core is composed of BAR domain proteins. *Mol. Biol. Cell.* 22:2360–2372.
20. Ziółkowska, N. E., L. Karotki, …, T. C. Walther. 2011. Eisosome-driven plasma membrane organization is mediated by BAR domains. *Nat. Struct. Mol. Biol.* 18:854–856.
21. Karotki, L., J. T. Huiskonen, …, T. C. Walther. 2011. Eisosome proteins assemble into a membrane scaffold. *J. Cell Biol.* 195:889–902.
22. Fröhlich, F., K. Moreira, …, T. C. Walther. 2009. A genome-wide screen for genes affecting eisosomes reveals Nce102 function in sphingolipid signaling. *J. Cell Biol.* 185:1227–1242.
23. Moreira, K. E., S. Schuck, …, P. Walter. 2012. Seg1 controls eisosome assembly and shape. *J. Cell Biol.* 198:405–420.
24. Elf, J., G. W. Li, and X. S. Xie. 2007. Probing transcription factor dynamics at the single-molecule level in a living cell. *Science.* 316:1191–1194.
25. Slaughter, B. D., J. W. Schwartz, and R. Li. 2007. Mapping dynamic protein interactions in MAP kinase signaling using live-cell fluorescence fluctuation spectroscopy and imaging. *Proc. Natl. Acad. Sci. USA.* 104:20320–20325.
26. Digman, M. A., R. Dalal, …, E. Gratton. 2008. Mapping the number of molecules and brightness in the laser scanning microscope. *Biophys. J.* 94:2320–2332.
27. Futcher, A. B., and B. S. Cox. 1984. Copy number and the stability of 2-micron circle-based artificial plasmids of *Saccharomyces cerevisiae*. *J. Bacteriol.* 157:283–290.
28. Digman, M. A., V. R. Caiolfa, …, E. Gratton. 2008. The phasor approach to fluorescence lifetime imaging analysis. *Biophys. J.* 94:L14–L16.
29. Hinde, E., M. A. Digman, …, E. Gratton. 2012. Biosensor Förster resonance energy transfer detection by the phasor approach to fluorescence lifetime imaging microscopy. *Microsc. Res. Tech.* 75:271–281.
30. Luo, G., A. Gruhler, …, R. C. Dickson. 2008. The sphingolipid long-chain base-Pkh1/2-Ypk1/2 signaling pathway regulates eisosome assembly and turnover. *J. Biol. Chem.* 283:10433–10444.
31. Mascaraque, V., M. L. Hernáez, …, M. Molina. 2013. Phosphoproteomic analysis of protein kinase C signaling in *Saccharomyces cerevisiae* reveals Slt2 mitogen-activated protein kinase (MAPK)-dependent phosphorylation of eisosome core components. *Mol. Cell. Proteomics.* 12:557–574.
32. Murphy, E. R., J. Boxberger, …, K. Kim. 2011. Pil1, an eisosome organizer, plays an important role in the recruitment of synaptojanins and amphiphysins to facilitate receptor-mediated endocytosis in yeast. *Eur. J. Cell Biol.* 90:825–833.
33. Fröhlich, F., R. Christiano, …, T. C. Walther. 2014. A role for eisosomes in maintenance of plasma membrane phosphoinositide levels. *Mol. Biol. Cell.* 25:2797–2806.

34. Dalal, R. B., M. A. Digman, …, E. Gratton. 2008. Determination of particle number and brightness using a laser scanning confocal microscope operating in the analog mode. *Microsc. Res. Tech.* 71:69–81.

35. Janke, C., M. M. Magiera, …, M. Knop. 2004. A versatile toolbox for PCR-based tagging of yeast genes: new fluorescent proteins, more markers and promoter substitution cassettes. *Yeast.* 21:947–962.

36. Unger, T., Y. Jacobovitch, …, Y. Peleg. 2010. Applications of the restriction free (RF) cloning procedure for molecular manipulations and protein expression. *J. Struct. Biol.* 172:34–44.

37. Digman, M. A., C. M. Brown, …, E. Gratton. 2008. Paxillin dynamics measured during adhesion assembly and disassembly by correlation spectroscopy. *Biophys. J.* 94:2819–2831.

Biophysical Journal

Supporting Material

Eisosomes Are Dynamic Plasma Membrane Domains Showing Pil1-Lsp1 Heteroligomer Binding Equilibrium

Agustina Olivera-Couto,[1] Valentina Salzman,[1] Milagros Mailhos,[1] Michelle A. Digman,[2,3] Enrico Gratton,[2,*] and Pablo S. Aguilar[1,*]

[1]Laboratorio de Biología Celular de Membranas, Institut Pasteur de Montevideo, Montevideo, Uruguay; [2]Laboratory for Fluorescence Dynamics, Department of Biomedical Engineering, University of California-Irvine, Irvine, California; and [3]Centre for Bioactive Discovery in Health and Ageing, School of Science and Technology, University of New England, Armidale, Australia

Supporting Materials and Methods:

S. cerevisiae strains, reagents, media and growth conditions:

Yeast strains were built from the w303 genetic background (*leu2-3,112 trp1-1 can1-100 ura3-1 ade2-1 his3-11,15*). pym25 and pym27 from EUROSCARF plasmid collection (1) where modified by RFcloning (2) substituting GFP open reading frame by monomeric Venus (mVenus) and monomeric Cerulean (mCerulean), respectively. mVenus and mCerulean open reading frames where taken from plasmids 27794 and 15214 (AddGene, Cambridge, MA). pym25-mVenus and pym27-mCerulean where used for C-terminal PCR based tagging of eisosomal proteins and pFA6a for PCR based gene deletion (1). Single tagged and single deletion strains where generated (Table S2) and checked by PCR and confocal microscopy. We combined different pairs of the former strains and performed matting, sporulation and tetrad dissections obtaining a set of strains with two chromosomal modifications (Table S2). Matting assays were performed in YPD plates (1% yeast extract (Becton Dickinson and Company, Franklin Lakes, NJ), 2% bacto-peptone (Becton Dickinson and Company, Franklin Lakes, NJ) and 2% glucose (Sigma-Aldrich, St. Louis, MO), 10% agar (Becton Dickinson and Company, Franklin Lakes, NJ)) at 30C overnight. Diploids were selected and incubated for sporulation over three days in SPO media (2.5 mg/L yeast extract, 150 mM potassium acetate (Sigma-Aldrich, St. Louis, MO), 1X complete supplement mixture (Sunrise Science Products, San Diego, CA) and 0.05% glucose (Sigma-Aldrich, St. Louis, MO)). Tetrads' dissection was performed in a dissection microscope (Singer Instrument, Somerset, UK); final strains were PCR and confocal microscopy checked. Using specific antibodies against Pil1 and western blotting, we verified that Pil1-mVenus protein levels were similar to Pil1 levels of the wild type strain w303 (Figure S6).

For mVenus cytoplasmic expression and Pil1-mVenus OE, pEG202 plasmid (generously given by Alejandro Colman Lerner) was used. It expresses lexA open reading frame under the control of *ADH1* gene promoter. We applied gap repair cloning technic to substitute lexA by mVenus or Pil1-mVenus open reading frames. For gap repair transformation in w303 yeast we linearized pEG202 with EcoRI and BamHI (New England Biolabs, Ipswich, MA) restriction enzymes.
In general, yeast strains were grown in 10 ml of complete media YPD to an OD600 between 0,8-1. For microscopy experiments, yeast cells were cultured (for a minimum of 18 hours) in SC complete defined media without Rivoflavin and Folic Acid (Sunrise Science Products, San Diego, CA) and supplemented with 80 ng/mL Adenine (Sigma-Aldrich, St. Louis, MO) at 30C to an optical density of 0.2-0.4. For imaging 200 uL of cell culture was incubated in Concanavalin-A (Sigma-Aldrich, St. Louis, MO) coated chambers for ten minutes (glass 1.5#) (Mat Tek Corporation, Ashland, MA). Finally, SC media was replaced for fresh one and cells were imaged.

Western blotting:

Cells were harvested by centrifugation and resuspended on 200 ul of 8 M Urea (Sigma-Aldrich, St. Louis, MO), 50 mM HEPES (Sigma-Aldrich, St. Louis, MO). Equal volume of 0,5 mm diameter glass beads were added to the resuspension, and cells where then subjected to 5 minutes agitation in bead beater (Genius). Once finished, 10 uL 10% SDS (Sigma-Aldrich, St. Louis, MO) were added and the mixture was incubated at 65C

for 5 minutes. After that time cellular derbies were pelleted by centrifugation for 10 minutes at 17 000 g, and the supernatant collected.

Total protein was measured using a commercially available BCA assay (Thermo Scientific, Waltham, MA) following the manufacturer's recommendations. Using BSA as the standard protein (Sigma-Aldrich, St. Louis, MO), a standard curve was prepared at levels 0.2, 0.4, 0.6, 0.8, 1.0 mg/mL. Samples were diluted in water as needed. Standards and sample dilutions were run in triplicate on 96-well plates (Corning Inc., Corning, NY). Buffer blanks were run in parallel and were used to correct for background. Plates were read on a multiscan microplate spectrophotometer (Thermo Scientific, Waltham, MA) at 570 nm.

For all samples 20 μg of total protein were subjected to 15% SDS–PAGE under reducing conditions and transferred onto a polyvinylidine difluoride membrane (PVDF, GE Healthcare, Wilmington, MA) that was blocked overnight at 4C with 5% non-fat dry milk in Tris Buffered Saline containing 0,05% Tween-20 (TBST, Sigma-Aldrich, St. Louis, MO). For immunoblotting, the membranes were incubated for 2h at room temperature with a polyclonal rabbit antiserum raised against recombinant purified Pil1 diluted 1:20000 or for loading control rabbit anti-Glucose-6-Phosphate Dehydrogenase antibody (Sigma-Aldrich, St. Louis, MO) diluted 1:20000 in TBST, 5% non-fat dry milk. The membranes were washed three times for 10 minutes with TBS-T. The horseradish peroxidase (HRP)-conjugated secondary goat anti-rabbit antibody (Sigma-Aldrich, St. Louis, MO) was used at a dilution of 1:16000 in TBS-T, 5% non-fat dry milk for 90 minutes and the membranes were subsequently washed three times for 10 minutes with TBS-T, developed using ECL Western Blotting Detection Reagent (GE Healthcare, Wilmington, MA) and exposed on a Hyperfilm ECL Chemiluminescence film (GE Healthcare, Wilmington, MA). Overexposure was in all cases prevented varying the exposure time. A pre-stained molecular mass marker ranging from 10 to 250 kDa were used to determine protein sizes (Thermo Scientific, Waltham, MA). ECL images were digitized using a SnapScan scanner (Agfa, Mortsel Belgium). Scanwise software was used to eliminate automatic grey scale adjustments done by the scanner to preserve linearity. Gel images were analysed using the ImageJ program (National Institutes of Health, NIH). Applying the "Rectangular Selection" tool a rectangular box was arbitrarily defined to the first lane and once defined the same box was used to measure all lanes present in the gel. The "Gel Analysis-Plot Lanes" function was used to draw a profile plot of each lane. The profile plot represents the relative density of the contents of the rectangle over each lane. Using the "Straight line" tool, a base line was drawn across each peak to enclose it and eliminate background and the "Wand" tool was applied to measure the area under the curve. Densities thus obtained for Pil1 were normalized with that obtained for G6PDH, and different mutants were analysed against WT. Since the values for Relative Density obtained are essentially arbitrary numbers, they only have meaning within the context of the set of peaks selected in a single gel image. For these reason, differences in protein expression were in all cases interpreted within a gel image.

Microscope setup:

A home-built two-photon excitation microscope based on an Olympus IX71 (Olympus Corporation, Tokyo, Japan) was used for all experiments (except for FLIM). The microscope was equipped with an Olympus UPlanFLN 60x water objective (NA=1.2)

(Olympus Corporation, Tokyo, Japan) and two photomultipliers detectors with a photon counting module H7422P-40 (Hamamatsu Photonics, Hamamatsu, Japan). The excitation light was provided by a mode-locked 80 MHz Ti:Sapphire laser Chameleon Ultra (Coherent Inc., Santa Clara, CA) with integrated Verdi tuneable from 690 to 1040 nm (for mVenus excitation 900 nm were used). We used a short-pass dichroic mirror 700DCSPXR (Chroma Technologies, Bellows Falls, VT) to direct the excitation light into the sample, and a 520BP-30 (Chroma Technoloies, Bellows Falls, VT) filter to select mVenus emission. The average laser irradiation after the microscope objective was the signal was amplified ACA-4-35N (Becker&Hickl, Berlin, Germany), a constant fraction discriminator model 6915 (Phillips Scientific, Mahwah, NJ) was used to convert the photon current in transistor–transistor logic (TTL) electronic pulses. Finally, the TTL pulses were counted using a FCS-PCI counter card version 0.2 (ISS, Champaign, IL). The scanning of the samples was performed using galvano motor-driven mirrors 6350 (Cambridge Technology Inc., Cambridge, MA) with a controller series 603X servo system 60335 FM (Cambridge Technology Inc., Cambridge, MA), and a PIFOC P-721 piezo-driven objective device (Physik Instrumente, Karlsruhe/Palmbach, Germany). Both galvano and piezo were driven by an 3-axis card (ISS, Champaign, IL).

Only for the FRET experiments, FLIM data was acquired with a Zeiss LSM710 META laser scanning microscope (Zeiss, Jena, Germany), coupled to a 2-photon Ti:Sapphire laser (Spectra-Physics Maitai, Newport, CA) producing 80 fs pulses at a repetition of 80 MHz, and a ISS A320 FastFLIM box (ISS, Champaign, IL) to acquire the lifetime data in the digital frequency domain. A 63X oil immersion objective 1.4 N.A. (Zeiss, Jena, Germany) was used. The 2-photon excitation laser was tuned to 850 nm for excitation of the donor and acceptor fluorophores. A SP 760 nm dichroic filter was used to separate the fluorescence signal from the laser light. The fluorescence signal was directed through a 509 LP filter, and the donor and acceptor signal split between two photomultiplier detectors H7422P-40 (Hamamatsu Photonics, Hamamatsu, Japan), with the following bandwidth filters in front of each: mCerulean 470/22 and mVenus 542/27, respectively. Pixel size of scanned images was 20 x 20 nm (x,y).

Mathematics and data processing:

All data was obtained and analyzed using SimFCS software (Laboratory for Fluorescence Dynamics, UCI, http://www.lfd.uci.edu/globals/, Irvine, CA). For specific statistical analysis like Gaussian fitting and boxplot constructions we also used MATLAB (The MathWorks, Inc., Natick, MA) and R (The R Foundation for Statistical Computing), respectively.

Number and Brightness analysis

Number (n) is defined as the average number of fluorescent molecules that were inside the observation volume during the pixel dwell time and molecular brightness (ε) as the average number of emitted photons per molecule per second when the molecule is at the centre of the PSF (Point Spread Function).

The brightness of a fluorescent molecule depends on a series of external factors including microscope laser and detectors. Also brightness depends on an intrinsic factor: the molecular oligomerization of the fluorescent particle observed. So if all the

cell external factors are constant we can use the brightness as a linear indicator of homo-oligomerization state when studying fluorescent-tagged proteins.

After sampling a pixel over time, N&B fluctuation analysis calculates these parameters from the average intensity at the pixel and the variance in the intensity distribution (3). For a given average, a large variance means that few bright molecules contributed to the average, while a small variance means that a high number of less bright molecules contributed to the average (3). Since we worked with a photon counting system it is not necessary to apply correction factors (4). The equations used to calculate B and N are:

$$B = \frac{\sigma^2}{\langle k \rangle} = \varepsilon + 1$$

$$N = \frac{\langle k \rangle^2}{\sigma^2} = \frac{\varepsilon n}{\varepsilon + 1}$$

where,

B is the apparent brightness
N is the apparent averaged number of molecules
$\langle k \rangle$ is the averaged intensity
σ^2 is the variance

For N&B analysis all the compared strains where imaged and processed exactly with the same method. Living yeast cells, concanavalin-A immobilized to the glass chamber, were observed by raster scan (256x256 pixel format, 36 nm pixel size) to focus the equatorial cell plane. An orbital scan of 30 pixel diameter was located in the image in order to scan cytoplasm, membrane, cell exterior, membrane and cytoplasm (Figure 1A). Circular scans were performed with 128 pixels along the circumference and a 16 μs pixel dwell time (orbital frequency of 488 Hz). The scan was repeated 20,480 times leading to a carpet of 128 columns. Pixel size in the orbit scan (calculated from pixel size of raster scan, orbit radius and number of pixels of the orbit) was 53 x 53 nm (x,y). Constant laser power was used between different scans and strains in the same day experiment. Intensity profiles across time were inspected for all the scans and a slow negative trend was detected due to photo-bleaching. In order to correct this trend we divided the carpets in segments of 10 seconds and we added to each segment random uncorrelated counts in order to match all segment mean count values with the intensity of the segment with most counts. The resultant detrended carpets were then free of slow trends due to photo-bleaching (3). Subsequently, intensity profiles were inspected again to verify that slow trends due to photo-bleaching were eliminated. Resulting orbital scanning records corresponding to the first half (10,240 orbits) were segmented into 128 smaller segments that were independently analyzed using the 'N and B' toolbox of SimFCS. In figures 2, 3, S3 and S4, I and B carpets show, in 128 consecutive rows, 128 independent N and B experiments for each scanned pixel. Each group of strains was analysed in a minimum of 3 independent experiments each consisting of a minimum of 6 scanned cells per strain.

For subcellular compartments definition the circular scan intensity profiles were used (Figure 3A). Gaussian fits were defined over intensity values and then we defined the eisosome core as the fluorescence centre of mass that encompasses the mean plus/minus

one standard deviations (SD) of the total eisosome fluorescence intensity signal, which, is in average, four pixels wide (212 nm). The remaining 30% of the signal was taken as signal providing mainly from the eisosome and surrounding space, what we have called eisosome edges (the three next contiguous pixels to the eisosome core) and the cytoplasmic compartment was defined as the central ten pixels (530 nm) wide area of cytoplasmic signal. Monomeric, oligomeric (from dimers to decamers) and multimeric B value ranges were defined in relation to mVenus B value distributions. Oligomer selection includes all pixels that have B values higher than the averaged monomer B value plus three SD and lower or equal to the averaged monomer B value plus 9 monomer molecular brightness (ε) values. All pixels with B values higher than oligomers were consider multimers.

Auto Correlation function (ACF):
For column ACF analysis the same sets of data than N&B analysis were used. Also point scans in the cytoplasm with scan frequencies of 50.000 or 100.000 Hz were analysed. For the time correlation, the time series was broken in segments and the average correlation function was calculated from the autocorrelation function of each segment. For ACF fitting three different models were applied: free diffusion of one component, free diffusion of two components and binding-unbinding equilibrium using the equations described in (5). ACF analysis and fittings were done using SimFCS software (Laboratory for Fluorescence Dynamics, UCI, http://www.lfd.uci.edu/globals/, Irvine, CA) and evaluated by χ^2 value (Table S1).

PSF calibration:
Due to the possible variation in the laser alignment from day to day PSF waist was calibrated for every experiment using fluorescein 10 nM in TRIS buffer pH 8, which has a known diffusion coefficient of 400 $\mu m^2/s$ at 25C. The value of w_z for two-photon experiments was assumed to five-times the radial waist.

FLIM-FRET analysis:
We performed *in vivo* Förster Resonance Energy Transfer (FRET) experiments using mVenus fluorescent tag as donor and mCerulean as acceptor. To detect the quenching of the donor's fluorescence lifetime during FRET phenomenon we used the phasor approach to fluorescence lifetime imaging microscopy (FLIM) (6, 7). Each pixel lifetime of the scanned cells was represented in the phasor plot using SimFCS software for analysis. The experimental position of the phasor of a given pixel along the trajectory determines the amount of quenching and therefore the FRET efficiency of that location. The contributions to the lifetime values of the background autofluorescence and of the unquenched donor are evaluated using the rule of the linear combination. Cells with no fluorescent tag were analysed for the background autofluorescence lifetime calibration and cells expressing either Pil1-mVenus or Lsp1-mVenus only were analysed for calibration of unquenched donor lifetime. To identify the subcellular source/s of the FRET signal we filtered, using the simFCS intensity histogram tool, the pixels corresponding to cytoplasm, eisosomes and eisosome edge compartments. In comparison to N&B segmentation, eisosome core and eisosome edges pixel values (and nanometers) are comparable. In the case of subcellular analysis we corroborated that the lifetime of donor only control was the same in all cell locations. For calculation of FRET efficiencies we considered unquenched mCerulean lifetimes in donor-only strains and background autofluorescence lifetimes in cells with no

fluorescent tag. Black circles encompass the pixel populations of the donor-only (0% FRET efficiency) and background controls. In all cases, at least 80% of the total pixel population was included within the circles. Encircled populations of pixels from these control strains were used to determine the expected FRET trajectories within the phasor plot using the 'assign' and 'FRET calculator' tools of SimFCS. The resulting FRET trajectories (see an example in Figure 4A, curved arrow in upper-left phasor plot) indicate the different expected positions within the phasor plot that correspond to different FRET efficiencies (from 0 to 100%). This calculation was done for each experiment and allowed to determine the FRET efficiency of the selected pixels populations among the different imaged strains. FRET efficiencies reported in Table 1 correspond to the value of efficiency of the calculated trajectory that intercepts the centre of mass of pixel lifetimes distributions coming from at least six different and independently imaged cells that were integrated in the same phasor plot. In the case of homotypic FRET analysis (Pil1-mCerulean Pil1-mVenus and Lsp1-mCerulean Lsp1-mVenus), FRET trajectory calculations also included the extra assumption that a 50% of the donor lifetimes could be unquenched due to interaction between donor-tagged proteins (Pil1-mCerulean-Pil1-mCerulean and Lsp1-mCerulean-Lsp1-mCerulean). Calculations were done using the SimFCS software developed at the Laboratory for Fluorescence Dynamics (www.lfd.uci.edu). Color coded representation of phasor plots of SimFCS is calibrated in a way that the centre of mass plus/minus one SD of the pixel dispersion is comprehended within the violet-colored pixels (which include the centre of mass) and the red-colored pixels, whereas two SD are contained between the violet- and the yellow-colored pixels. Details about the mathematical equations considered for the phasor transformation and FRET efficiency calculations can be found in previously published papers (6, 7).

Supporting Tables:

Table S1. Eisosome edge ACF free diffusion or binding-unbinding equilibrium fittings

Lsp1	**Binding**			**Free diffusion**			
	k	**A**	**χ^2**	**D**	**$G_{(0)}$**	**χ^2**	**χ^2 ratio**
1	4.2	0.006	6.7115E-06	0.0078	0.059	6.8185E-06	1.02
2	2.9	0.0028	2.3197E-06	0.03	0.003	2.3919E-06	1.03
3	4	0.0047	4.1265E-06	0.05	0.0054	4.2686E-06	1.03
4	2.9	0.0036	5.1873E-06	0.034	0.0039	5.2988E-06	1.02
5	3.8	0.0026	2.7405E-06	0.082	0.004	4.3752E-06	1.60
6	3.4	0.0027	1.7313E-06	0.074	0.003	1.8116E-06	1.05
7	2.6	0.043	5.10655E-05	0.033	0.051	5.53492E-05	1.08
8	1.6	0.011	0.000028152	0.022	0.0044	3.59926E-05	1.28
9	2.8	0.0038	1.34956E-05	0.026	0.0042	1.36259E-05	1.01
10	2	0.0058	1.22081E-05	0.031	0.0069	1.22317E-05	1.00
11	4.1	0.0048	0.000013067	0.047	0.0054	1.32089E-05	1.01
Mean	**3.1**	**0.01**		**0.04**	**0.01**		**1.1**
SD	**0.9**	**0.01**		**0.02**	**0.02**		**0.2**
Pil1	**Binding**			**Free diffusion**			
	k	**A**	**χ^2**	**D**	**$G_{(0)}$**	**χ^2**	**χ^2 ratio**
1	4.1	0.034	5.5572E-06	0.067	0.038	9.38885E-06	1.69

2	2.1	0.011	8.1859E-06	0.058	0.012	8.5432E-06	1.04
3	2.9	0.0022	1.0944E-06	0.13	0.0025	1.1614E-06	1.06
4	3.1	0.037	5.32655E-05	0.11	0.039	6.70371E-05	1.26
5	2.3	0.025	9.33019E-05	0.05	0.031	9.46982E-05	1.01
6	2.4	0.052	0.356104555	0.34	0.094	0.384338149	1.08
7	2.5	0.0031	8.439E-07	0.074	0.0035	8.906E-07	1.06
8	3.6	0.0016	1.3121E-06	0.14	0.0019	1.3164E-06	1.00
9	2.7	0.0022	1.6156E-06	0.01	0.0024	1.6915E-06	1.05
10	3.5	0.0043	8.8	0.23	0.0052	9.3	1.06
Mean	**2.9**	**0.02**		**0.2**	**0.02**		**1.1**
SD	**0.6**	**0.02**		**0.1**	**0.03**		**0.2**

Yeast strains expressing Lsp1-mVenus and Pil1-mVenus (top and bottom panels) where analyzed by circular scans and carpet columns corresponding to eisosome edges showed ACF. These ACF were fitted by two different models, free diffusion (characterized by $G_{(0)}$ and D (in $\mu m^2/s$)) and binding-unbinding equilibrium (characterized by amplitude A and rate k (in s^{-1})). Each fit provides a χ^2 value. The ratio of the χ^2 values for the fit using the binding-unbinding equation and the diffusion equation are reported in the last column.

Table S2. Yeast strains used in this work

Strain	Relevant genotype	Source
PSAY1240	W303 *MATa* carrying pEG202mVenus (HIS3 ADH1p-mVENUS).	This work.
PSAY1133	W303 *MATα PIL1-mVENUS-hphNT1*.	This work.
PSAY1019	W303 *MATα PIL1-mCERULEAN-kanMX4*..	This work.
PSAY1041	W303 *MATα* LSP1-mVENUS-*hphNT1*.	This work.
PSAY1040	W303 *MATα* LSP1-mCERULEAN-*kanMX4*..	This work.
PSAY1245	W303 *MATa pil1*::caLeu pEG202-Pil1mVenus-HIS.	This work.
PSAY1194	W303 *MATa lsp1::NAT* PIL1-mVENUS-*hphNT1*.	This work.
PSAY1059	W303 *MATα* PIL1-mCERULEAN-*kanMX4*. LSP1-mVENUS-*hphNT1*.	This work.
PSAY1127	W303 *MATα* LSP1-mCERULEAN-*kanMX4*. PIL1-mVENUS-*hphNT1*.	This work.
PSAY1132	W303 *MATdiploid* PIL1-mCERULEAN-*kanMX4*./PIL1-mCERULEAN-*kanMX4*..	This work. This work.
PSAY1091	W303 *MATdiploid* LSP1-mCERULEAN-*kanMX4*. /LSP1-mCERULEAN-*kanMX4*..	This work.
PSAY1132	W303 *diploid* PIL1-mCERULEAN-*kanMX4*. PIL1-mVENUS-*hphNT1*.	This work.
PSAY1307	W303 *diploid lsp1::NAT/lsp1::NAT* PIL1-mCERULEAN-*kanMX4*./PIL1-mVENUS-*hphNT1*.	This work.
PSAY1091	W303 *diploid* LSP1-mCERULEAN-*kanMX4*./LSP1-mVENUS-*hphNT1*.	This work.

Supporting references:

1. Janke, C., M. M. Magiera, N. Rathfelder, C. Taxis, S. Reber, H. Maekawa, A. Moreno-Borchart, G. Doenges, E. Schwob, E. Schiebel, and M. Knop. 2004. A versatile toolbox for PCR-based tagging of yeast genes: new fluorescent proteins, more markers and promoter substitution cassettes. Yeast 21:947-962.
2. Unger, T., Y. Jacobovitch, A. Dantes, R. Bernheim, and Y. Peleg. 2010. Applications of the Restriction Free (RF) cloning procedure for molecular manipulations and protein expression. J Struct Biol 172:34-44.
3. Digman, M. A., R. Dalal, A. F. Horwitz, and E. Gratton. 2008. Mapping the number of molecules and brightness in the laser scanning microscope. Biophys J 94:2320-2332.
4. Dalal, R. B., M. A. Digman, A. F. Horwitz, V. Vetri, and E. Gratton. 2008. Determination of particle number and brightness using a laser scanning

confocal microscope operating in the analog mode. Microsc Res Tech 71:69-81.
5. Digman, M. A., C. M. Brown, A. R. Horwitz, W. W. Mantulin, and E. Gratton. 2008. Paxillin dynamics measured during adhesion assembly and disassembly by correlation spectroscopy. Biophys J 94:2819-2831.
6. Digman, M. A., V. R. Caiolfa, M. Zamai, and E. Gratton. 2008. The phasor approach to fluorescence lifetime imaging analysis. Biophys J 94:L14-16.
7. Hinde, E., M. A. Digman, C. Welch, K. M. Hahn, and E. Gratton. 2012. Biosensor Forster resonance energy transfer detection by the phasor approach to fluorescence lifetime imaging microscopy. Microsc Res Tech 75:271-281.

Supplemental Figures:

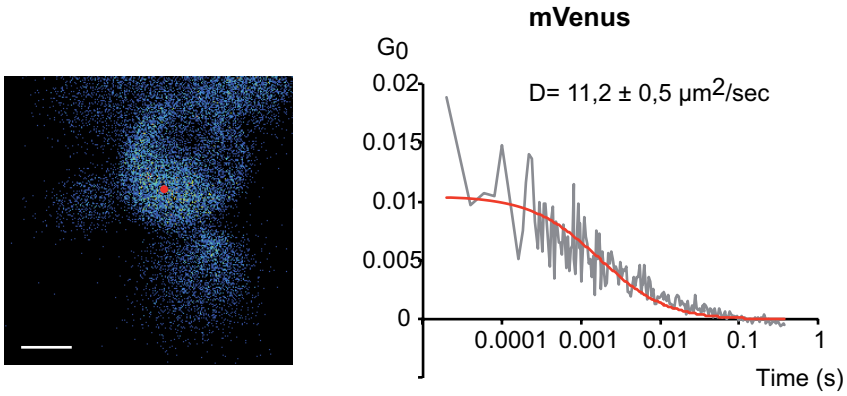

Figure S1. Autocorrelation function (ACF) analysis of cytoplasmic monomeric Venus. Representative image, ACF plot and free diffusion fitting of data coming from mVenus-containing yeast cells that were subjected to point scans. The red dot indicates the laser bin position for this particular case. Scale bar: 2 μm.

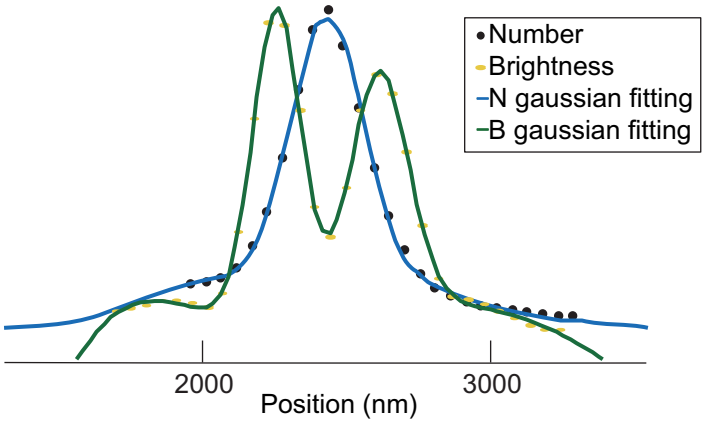

Figure S2. Eisosome edges Pil oligomers localization. For determining the distance between the eisosome core and the oligomers, a Gaussian fit for the N and B distributions as a function of the position from the eisosome centre was done. An example of the B vs. position (yellow dots) and N vs. position (black dots) plots are shown with their respective Gaussian fits (blue and green lines).

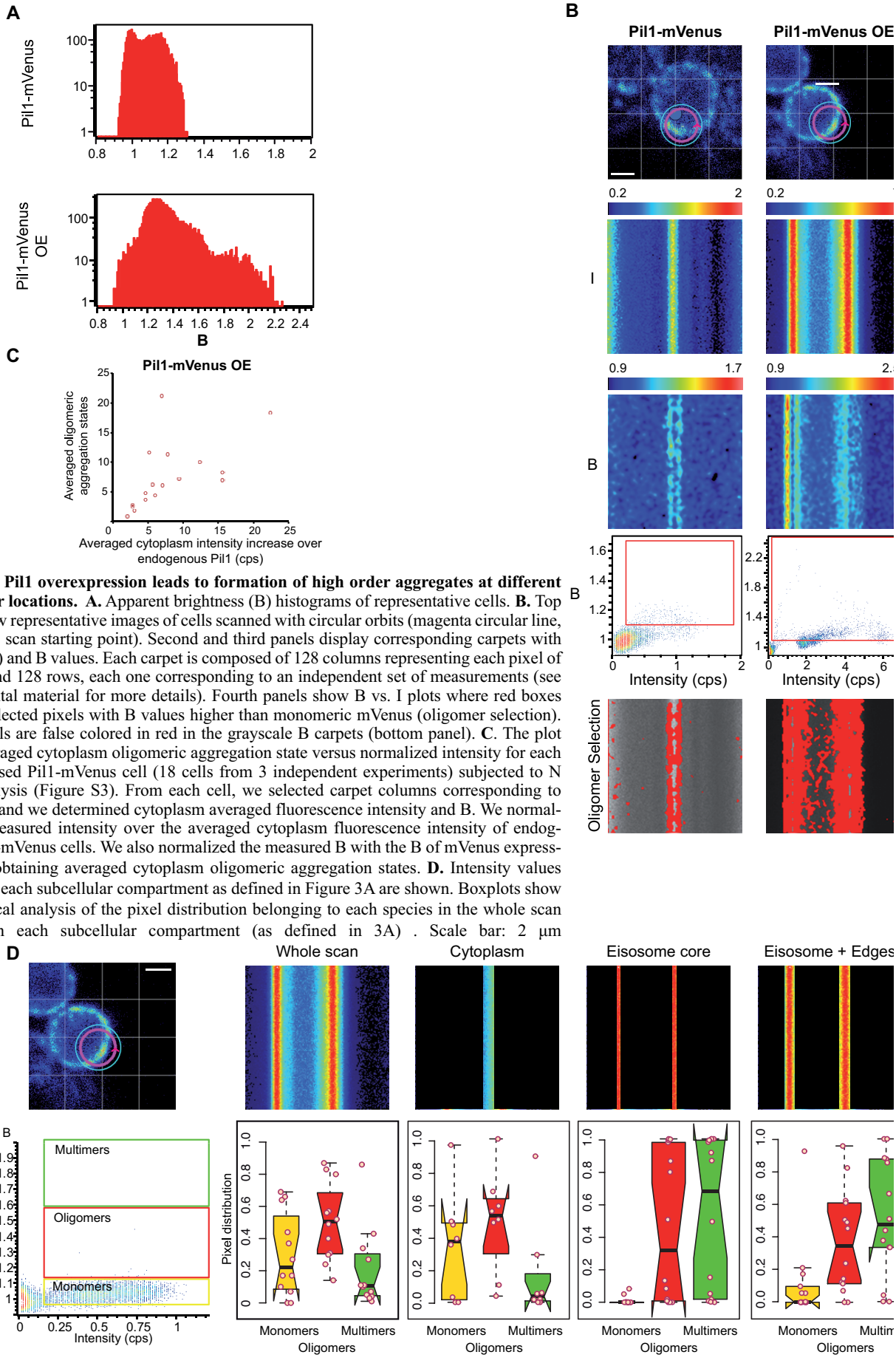

Figure S3. Pil1 overexpression leads to formation of high order aggregates at different subcellular locations. A. Apparent brightness (B) histograms of representative cells. **B.** Top panels show representative images of cells scanned with circular orbits (magenta circular line, arrowhead: scan starting point). Second and third panels display corresponding carpets with intensity (I) and B values. Each carpet is composed of 128 columns representing each pixel of the orbit and 128 rows, each one corresponding to an independent set of measurements (see Supplemental material for more details). Fourth panels show B vs. I plots where red boxes indicate selected pixels with B values higher than monomeric mVenus (oligomer selection). These pixels are false colored in red in the grayscale B carpets (bottom panel). **C**. The plot shows averaged cytoplasm oligomeric aggregation state versus normalized intensity for each overexpressed Pil1-mVenus cell (18 cells from 3 independent experiments) subjected to N and B analysis (Figure S3). From each cell, we selected carpet columns corresponding to cytoplasm and we determined cytoplasm averaged fluorescence intensity and B. We normalized the measured intensity over the averaged cytoplasm fluorescence intensity of endogenous Pil1-mVenus cells. We also normalized the measured B with the B of mVenus expressing cells, obtaining averaged cytoplasm oligomeric aggregation states. **D.** Intensity values carpets for each subcellular compartment as defined in Figure 3A are shown. Boxplots show the statistical analysis of the pixel distribution belonging to each species in the whole scan and within each subcellular compartment (as defined in 3A) . Scale bar: 2 µm

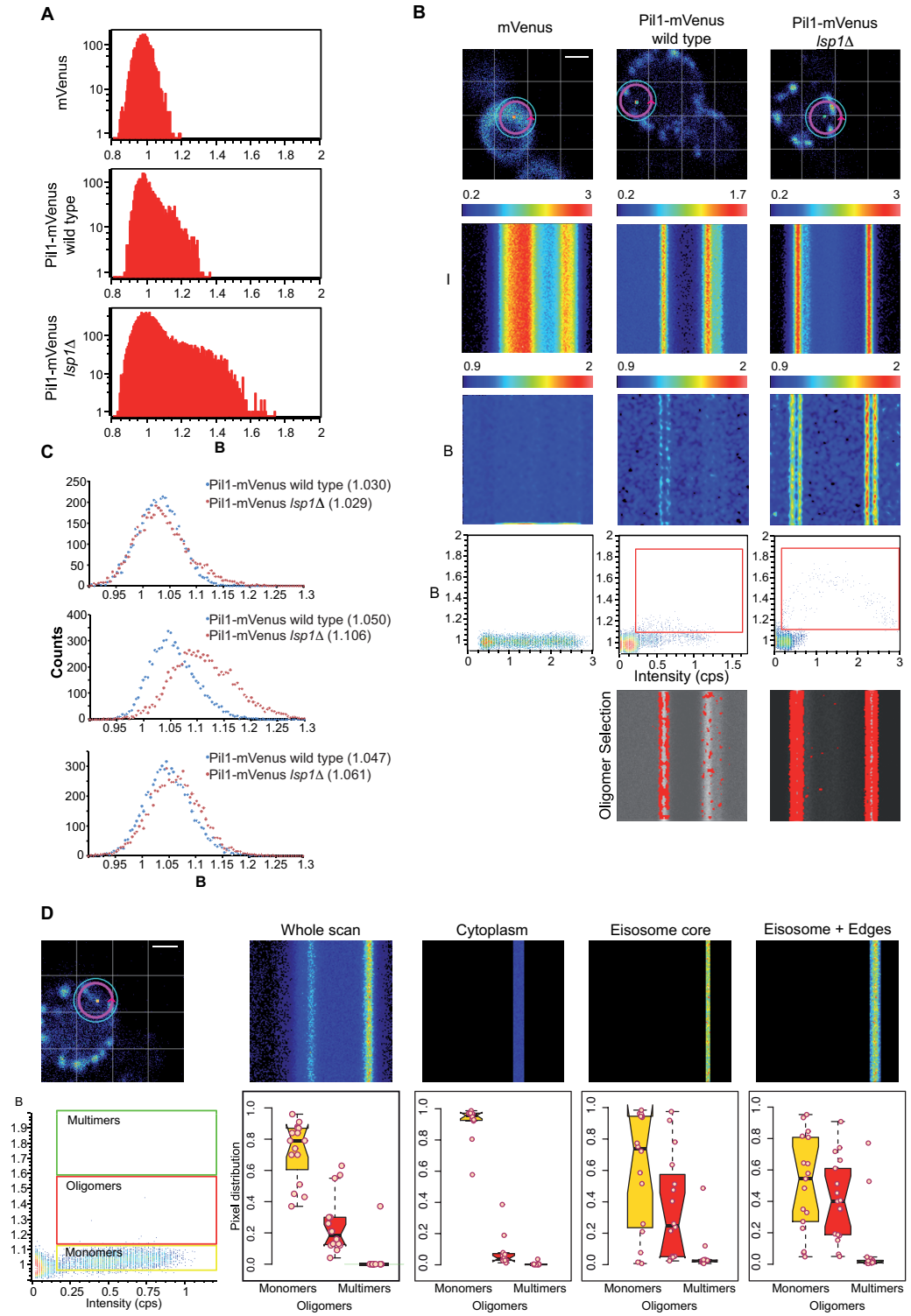

Figure S4: In the absence of Lsp1, there is an increase in Pil1 oligomers. Yeast *lsp1*Δ cells carrying Pil1-mVenus were subjected to circular scans and N&B analysis. **A.** Apparent brightness (B) histograms of representative wild type mVenus, wild type Pil1-mVenus and *lsp1*Δ Pil1-mVenus cells. **B.** Top panels show representative images of cells scanned with circular orbits (magenta circular line, arrow-head: scan starting point). Second and third panels display corresponding intensity (I) and B carpets. Each carpet is composed of 128 columns representing each pixel of the orbit and 128 rows, each one corresponding to an independent set of measurements (see Supplemental material for more details). Fourth panels show B vs. I plots where red boxes indicate selected pixels with B values higher than monomeric mVenus. These pixels are false colored in red in the grayscale B carpets (bottom panel). **C.** Pil1-mVenus cytoplasmic B values of wild type and *lsp1*Δ cells. Within each independent experiment the histograms of Pil1-mVenus cytoplasmic B values of individual cells (at least 6 cells/experiment) were accumulated generating one integrated histogram per independent experiment (3 panels). For each integrated histogram a Gaussian fit was performed to extract the positions of the mean (values between parentheses). **D.** Intensity values carpets for each subcellular compartment as defined in Figure 3A are shown. Boxplots show the statistical analysis of the pixel distribution belonging to each species in the whole scan and within each subcellular compartment (as defined in 3A) of Pil1-mVenus *lsp1*Δ cells. Data from three independent experiments with at least six cells per experiment were analyzed. Scale bar: 2 µm.

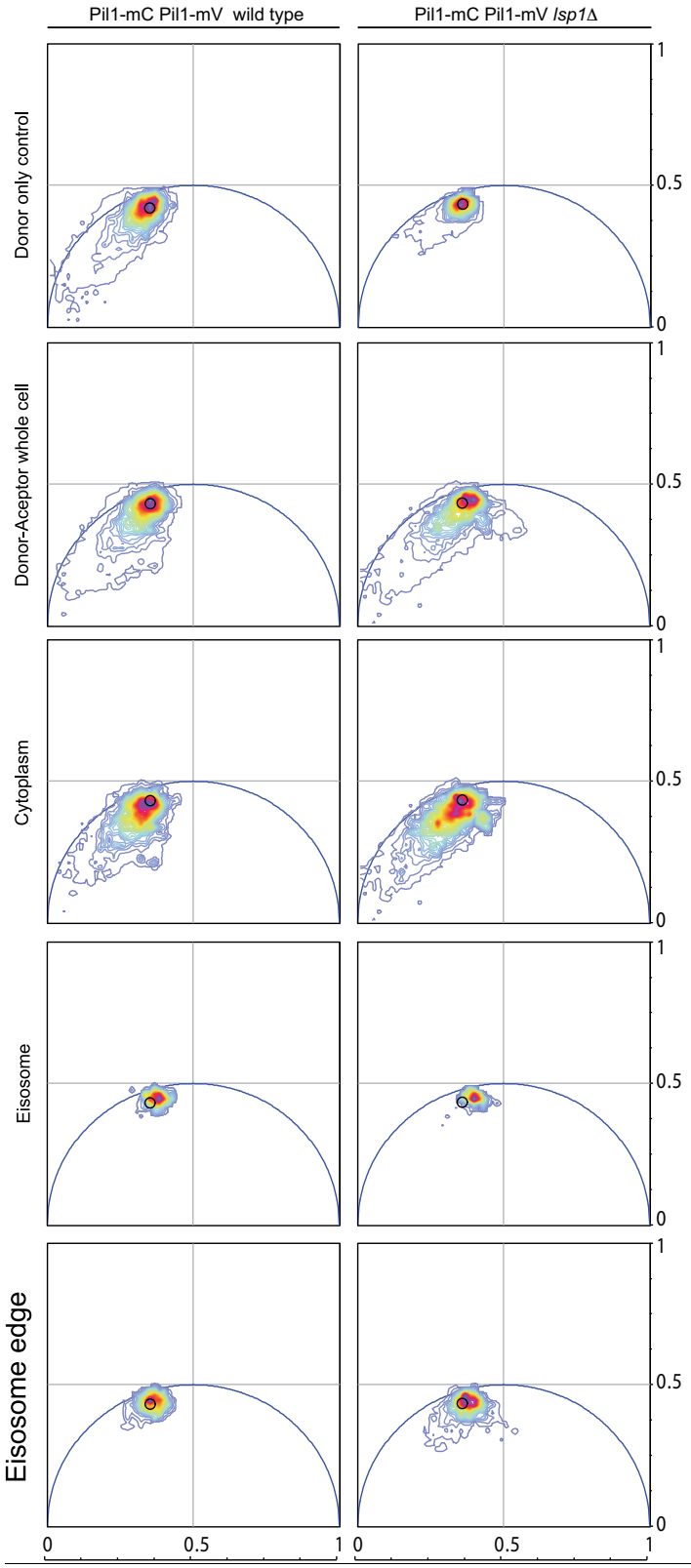

Figure S5. Lsp1 deletion allows cytoplasmic Pil1 homotypic interaction. Pil1-mCerulean Pil1-mVenus wild type (left panel) and Pil1-mCerulean Pil1-mVenus *lsp1*Δ (right panel) cells where imaged with a 2-photon microscope equipped with a FLIM box. Yeast strains expressing the fluorescent donor Pil1-mCerulean only were used as negative controls (upper panels). Black circle is concentric to donor-only pixel distribution center of mass and encompass the 80% of pixels. Phasor plots of pixels lifetimes corresponding to the whole cell and different subcellular compartments as defined in Figure 4B are shown. Phasor plots with pixel distributions lifetimes were built from the integration of 6 or more cells in each plot. The black circle indicates the position of the centre of mass of the donor only control pixel distribution. From violet until red colour one standard deviation of the pixel dispersion is comprehended, and two standard deviations are contained until yellow.

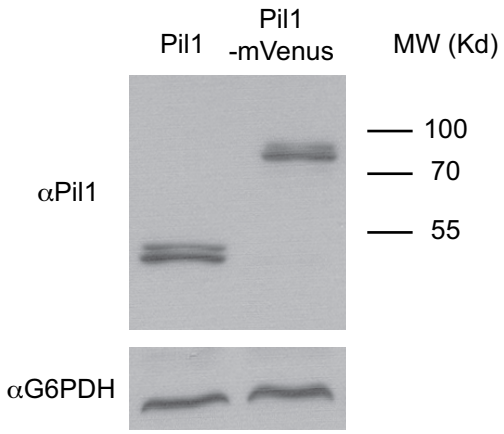

Figure S6. Pil1-mVenus expression levels control. Wild type and Pil1-mVenus cells were grown, harvested and total protein extracts were subjected to Western blotting using a-Pil1 polyclonal antiserum (α-Pil1). For a loading control, an a-Glucose-6-Phosphate Dehydrogenase antibody (α-G6PDH) was used.